AGU PUBLICATIONS

JGR

Journal of Geophysical Research: Oceans

RESEARCH ARTICLE

10.1002/2016JC012650

Special Section:

The Southern Ocean Carbon and Climate Observations and Modeling (SOCCOM) Project: Technologies, Methods, and Early Results

Key Points:

- A biogeochemical state estimate of the Southern Ocean is produced for 2008–2012
- The estimate captures the variability of Drake Passage pCO_2 and oxygen profiles from Argo floats
- Validity of the adjoint method for the coupled model is demonstrated through sensitivity experiments

Correspondence to:

A. Verdy,
averdy@ucsd.edu

Citation:

Verdy, A. and M. R. Mazloff (2017), A data assimilating model for estimating Southern Ocean biogeochemistry, *J. Geophys. Res. Oceans*, *122*, 6968–6988, doi:10.1002/2016JC012650.

Received 21 DEC 2016
Accepted 21 JUL 2017
Accepted article online 15 AUG 2017
Published online 1 SEP 2017

A data assimilating model for estimating Southern Ocean biogeochemistry

A. Verdy[1] and **M. R. Mazloff**[1]

[1]Scripps Institution of Oceanography, La Jolla, California, USA

Abstract A Biogeochemical Southern Ocean State Estimate (B-SOSE) is introduced that includes carbon and oxygen fields as well as nutrient cycles. The state estimate is constrained with observations while maintaining closed budgets and obeying dynamical and thermodynamic balances. Observations from profiling floats, shipboard data, underway measurements, and satellites are used for assimilation. The years 2008–2012 are chosen due to the relative abundance of oxygen observations from Argo floats during this time. The skill of the state estimate at fitting the data is assessed. The agreement is best for fields that are constrained with the most observations, such as surface pCO_2 in Drake Passage (44% of the variance captured) and oxygen profiles (over 60% of the variance captured at 200 and 1000 m). The validity of adjoint method optimization for coupled physical-biogeochemical state estimation is demonstrated with a series of gradient check experiments. The method is shown to be mature and ready to synthesize in situ biogeochemical observations as they become more available. Documenting the B-SOSE configuration and diagnosing the strengths and weaknesses of the solution informs usage of this product as both a climate baseline and as a way to test hypotheses. Transport of Intermediate Waters across 32°S supplies significant amounts of nitrate to the Atlantic Ocean (5.57 ± 2.94 Tmol yr^{-1}) and Indian Ocean (5.09 ± 3.06 Tmol yr^{-1}), but much less nitrate reaches the Pacific Ocean (1.78 ± 1.91 Tmol yr^{-1}). Estimates of air-sea carbon dioxide fluxes south of 50°S suggest a mean uptake of 0.18 Pg C/yr for the time period analyzed.

1. Introduction

Argo floats equipped with biogeochemical sensors (bgc-Argo) are providing unprecedented coverage of the Southern Ocean carbon system. Float data are being used to estimate air-sea fluxes of CO_2 [*Williams et al.*, 2017] and net community production [*Plant et al.*, 2016; *Johnson et al.*, 2017]. Still, observations are too sparse to provide the coverage and resolution needed for quantifying basin-scale patterns and variability [*Gruber*, 2009; *Lovenduski et al.*, 2015]. Numerical models are useful tools for assessing the physical and biological mechanisms driving the observed variability in the ocean carbon system. However, state-of-the-art ocean general circulation models and Earth system models tend to disagree widely in their assessment of the physical state and biogeochemistry in the Southern Ocean [*Bopp et al.*, 2013; *Sallée et al.*, 2013; *Jiang et al.*, 2014] due to their sensitivity to domain configuration, choice of initial conditions, internal parameterizations, and atmospheric state, all of which are poorly constrained by observations. State estimation provides a means to bring a numerical model into consistency with the available data, producing a hindcast of the ocean state that is dynamically consistent and that has closed budgets for carbon and other biogeochemical tracers [*Wunsch and Heimbach*, 2013].

The Southern Ocean State Estimate (SOSE) [*Mazloff et al.*, 2010] has been developed to provide an ocean climate baseline and to be a science resource for understanding the physics controlling ocean properties. The state estimate is produced by solving for the model initial and boundary conditions, so-called model “controls,” that minimize a weighted least squares sum of model-observation misfits. This is achieved using an adjoint model that provides the gradients of the misfits function with respect to the model controls, allowing those controls to be efficiently and systematically determined. The advantage of the adjoint method (or 4D-Var) data assimilation approach is that the numerical model propagates observational information across variables using model dynamics. These dynamics include complex processes, such as mixed layer depth variability, that govern the ocean carbon system. Because the adjoint method does not involve unphysical nudging terms, agreement of the solution with observations is not guaranteed, but requires consistency with the model equations and closed internal budgets.

Data assimilation with biogeochemical or ecosystem modeling has proven challenging due to the paucity of data and complexity of the system [*Matear*, 1995; *Fennel et al*., 2001; *Friedrichs et al*., 2006]. Examples of the application of the adjoint method include *Schlitzer* [2002], *Faugeras et al*. [2003], *Song et al*. [2012], *Doi et al*. [2015], *Song et al*. [2016a,2016b], and *Mattern et al*. [2017]. Efforts have been mainly focused on estimating model parameters. In addition to data assimilation, the adjoint method can be used for sensitivity analyses; the study by *Dutkiewicz et al*. [2006] analyzes the sensitivity of global air-sea CO_2 fluxes using the adjoint of a coupled physical-biogeochemical model.

By implementing a biogeochemical model into the SOSE framework and constraining to observations, we have produced a biogeochemical Southern Ocean State Estimate (B-SOSE; http://sose.ucsd.edu) for the years 2008–2012. This period is chosen for the relative abundance of biogeochemical in situ observations primarily due to a large number of Argo floats with oxygen sensors being released in the Southern Ocean in 2007 and 2008. These data were recently calibrated and made available at http://runt.ocean.washington.edu/o2/. B-SOSE was conceived with the central purpose of attaining a best estimate of the large-scale carbon system properties of the Southern Ocean. It was also produced acknowledging that a biogeochemical assimilation infrastructure must be developed in support of the influx of measurements currently being collected by floats deployed by the Southern Ocean Carbon and Climate Observations and Modeling (SOCCOM; http://soccom.princeton.edu) project. SOCCOM is deploying approximately 25 floats/yr in the Southern Ocean with nitrate, oxygen, pH, and optical sensors. Thus the focus of the paper is on presenting not just the B-SOSE solution, but also the methodology. In section 2, we describe the model, the observational constraints, and the model controls. In section 3, we evaluate the accuracy of the adjoint model. The state estimate solution is presented in section 4, along with a quantitative assessment of the fit to observations. In section 5, we give examples of the utility of the B-SOSE solution. Concluding remarks are given in section 6.

2. Methods

We implement the Biogeochemistry with Light, Iron, Nutrients, and Gases model (BLING) [*Galbraith et al*., 2010] into the SOSE framework, which is based on the MIT general circulation model (MITgcm; evolved from *Marshall et al*. [1997]) and the software developed by the consortium for Estimating the Circulation and Climate of the Ocean (ECCO) [*Stammer et al*., 2002; *Wunsch and Heimbach*, 2013]. The B-SOSE domain has an open boundary at the equator, and the analysis focuses on the solution poleward of 30°S (Figure 1). We describe the physical setup in section 2.1 as it differs from that described in *Mazloff et al*. [2010]. Our implementation of BLING is described in section 2.2. An overview of the data assimilation methodology is given in section 2.3. Observational constraints and model controls are presented in sections 2.4 and 2.5, respectively.

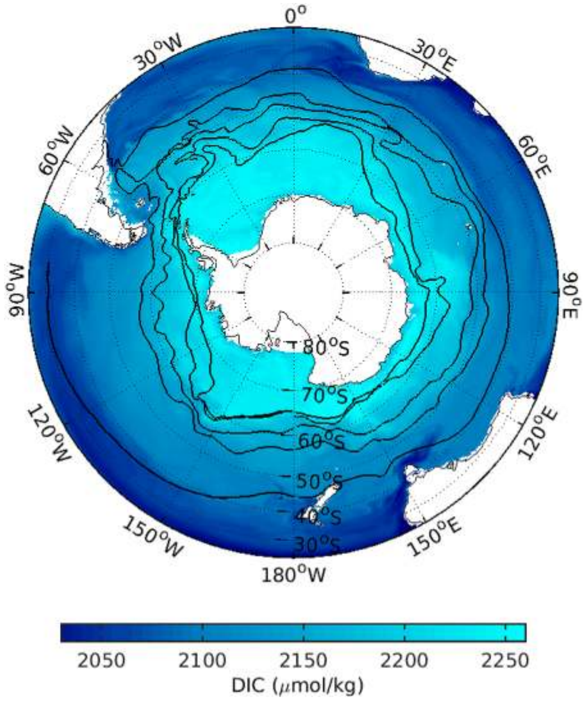

Figure 1. Snapshot of the simulated dissolved inorganic carbon (DIC) concentration at 100 m on 1 February 2009. Black contours show the mean position of Antarctic Circumpolar Current fronts [*Orsi et al*., 1995]. The B-SOSE domain has an open boundary at the equator, and the analysis here focuses on the solution poleward of 30°S.

2.1. Physical Model Configuration

B-SOSE is an unprecedented space and time resolved estimate of Southern Ocean biogeochemistry, including air-sea fluxes of heat and carbon and cycling of nutrients. Our future goal is eddy resolution; however, at these preliminary stages of biogeochemical state estimation, it is practical to focus on reproducing the largest scales. Due to this initial goal, and to save computational cost, we use a model with relative coarse 1/3°

Table 1. Ocean and Biogeochemical Model Parameters

Ocean Model Parameters		
Δx	Horizontal resolution	1/3°
Δz	Vertical resolution	4.2–400 m
Δt	Time step	1 h
	Ocean lateral open boundary forcing period	1 month
	Atmospheric boundary forcing period	6 h
	Horizontal viscosity	$10\ \mathrm{m}^2\ \mathrm{s}^{-1}$
	Horizontal diffusivity	$10\ \mathrm{m}^2\ \mathrm{s}^{-1}$
	Vertical viscosity	$1\times10^{-3}\ \mathrm{m}^2\ \mathrm{s}^{-1}$
	Vertical diffusivity	$1\times10^{-4}\ \mathrm{m}^2\ \mathrm{s}^{-1}$
Biogeochemical Model Parameters		
μ_0	Maximum phytoplankton photosynthesis rate at 0°C	$1.1\ \mathrm{d}^{-1}$
μ_{0d}	Maximum diazotroph photosynthesis rate at 0°C	$0.007\ \mathrm{d}^{-1}$
k_{PO_4}	Phosphate half-saturation coefficient	1×10^{-4} mol P/m^3
k_{NO_3}	Nitrate half-saturation coefficient	2×10^{-3} mol N/m^3
k_{Fe}	Iron half-saturation coefficient	4×10^{-7} mol Fe/m^3
k_{Fed}	Iron half-saturation coefficient for diazotrophs	3.5×10^{-7} mol Fe/m^3
C:N	Carbon to nitrogen stoichiometric ratio	6.75
O:N	Oxygen to nitrogen stoichiometric ratio	9.5
P:N	Phosphorus to nitrogen stoichiometric ratio (variable)	0.035–0.11
Fe:N	Iron to nitrogen stoichiometric ratio (variable)	$1.35–16.8\times10^{-5}$
λ_0	Constant in loss rate function	$0.19\ \mathrm{d}^{-1}$
B_0	Constant in loss rate function (pivotal biomass)	2.8×10^{-4} mol N/m^3
κ	Temperature dependence constant [*Eppley*, 1972]	0.063° C^{-1}
κ_d	Temperature dependence constant for diazotrophs	0.18° C^{-1}
γ_{DON}	Remineralization rate for DON	$0.25\ \mathrm{yr}^{-1}$
γ_{DOP}	Remineralization rate for DOP	$0.5\ \mathrm{yr}^{-1}$

horizontal resolution. The state estimate, therefore, lacks much of the important mesoscale dynamics, implying heightened model error in representing property transport and mixing.

The model domain extends from the equator to 78°S. The zonal grid spacing is always 1/3°, but the meridional grid spacing changes with latitude: poleward of 30°S, the model is configured on a Mercator projection ($\Delta y = \Delta x$), and equatorward of 30°S the meridional spacing telescopes out to reach $\Delta y = 2°$ at the equator. The setup uses 52 vertical levels of varying thickness. The bathymetry and coastline are derived from ETOPO1 [*Amante and Eakins*, 2009]. The governing equations are stepped forward with a 1 h time step and a third-order direct space and time advection scheme. The ocean is forced through an atmospheric boundary layer scheme where fluxes of heat, freshwater (salt), and momentum are determined by bulk formulae [*Large and Yeager*, 2009]. Six hourly atmospheric conditions from ERA-Interim [*Dee et al.*, 2011] are applied, and this atmospheric state is adjusted using the adjoint method. Initial conditions are also optimized, with first-guess fields derived from a global 1° resolution state estimate [*Forget et al.*, 2015] and the 1/6° SOSE solution [*Mazloff et al.*, 2010]. The prescribed open boundary conditions at the equator are derived from HYCOM (http://hycom.org). River runoff comes from the product of *Dai and Trenberth* [2002] augmented with an estimate of Antarctic continental runoff produced by *Hammond and Jones* [2016]. Tidal forcing is not included. Sea ice is modeled as described in *Losch et al*. [2010] and *Fenty and Heimbach* [2012]. The GGL90 mixed layer parameterization is used [*Gaspar et al*., 1990]; mesoscale eddy parameterization is not included. Horizontal and vertical viscosity and diffusivity parameters are given in Table 1.

2.2. Biogeochemical Model Configuration

The biogeochemical component, schematized in Figure 2, is adapted from the BLING model of *Galbraith et al*. [2010]. BLING was designed as a model of intermediate complexity for realistic simulations of large-scale ocean biogeochemistry. The version employed here includes eight prognostic tracers, a relatively small number, and an idealized representation of ecosystem dynamics. It is well suited for state estimation because (1) it is computationally inexpensive to run, (2) it includes relatively few parameters, and (3) it explicitly simulates the biogeochemical tracers measured by SOCCOM floats: oxygen, nitrate, and pH.

The original BLING model described in *Galbraith et al*. [2010] has been modified with the addition of nitrogen cycling and improvements to the representation of phytoplankton population dynamics and particle export [*Galbraith et al*., 2015; *Bianchi et al*., 2013]. We have added the code into the MITgcm repository after

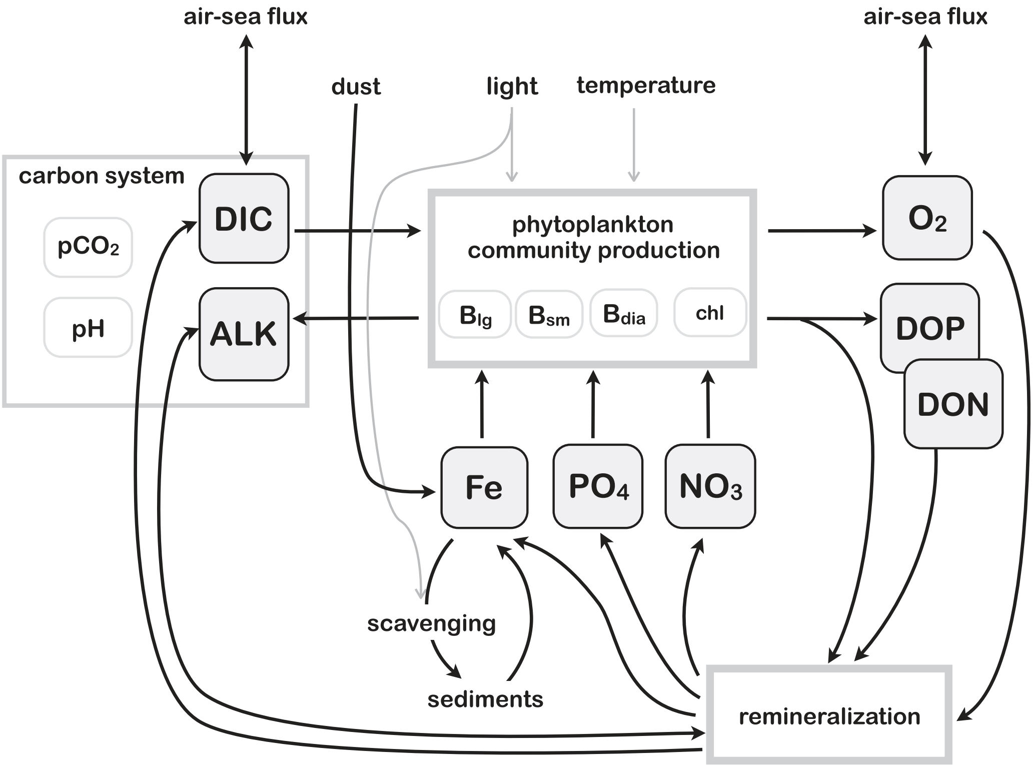

Figure 2. Schematic of the biogeochemical model. There are eight prognostic variables (gray shaded boxes): dissolved inorganic carbon (DIC), alkalinity (ALK), oxygen (O_2), nitrate (NO_3), phosphate (PO_4), iron (Fe), and dissolved organic matter (DON, DOP). Phytoplankton biomass, chlorophyll (chl), pH, and pCO_2 are diagnosed from the prognostic variables. The phytoplankton community includes three types of organisms: large diatom-like cells (B_{lg}), small calcifying cells (B_{sm}), and diazotrophs (B_{dia}). Community production is limited by the availability of light and nutrients and modulated by temperature. Uptake and remineralization of nutrients, as well as changes in oxygen and alkalinity, are calculated from the uptake and remineralization of nitrate via stoichiometric ratios. Black arrows represent fluxes and gray arrows indicate external forcing.

making it compatible with the automatic differentiation software used to produce the adjoint model (Transformation of Algorithms in Fortran, http://www.fastopt.com/products/taf/). It is available for public use at http://mitgcm.org.

The model includes a full description of the carbon system, adapted from the MITgcm simple biogeochemical model [*Dutkiewicz et al*., 2006]. Dissolved inorganic carbon (DIC) and alkalinity (ALK) are prognostic variables, and pH and pCO_2 are diagnosed based on *Follows et al*. [2006]. Air-sea fluxes of CO_2 and oxygen (O_2) are calculated following *Wanninkhof* [1992]. Atmospheric pCO_2 is prescribed from the CarbonTracker product [*Peters et al*., 2007].

Biological activity influences the concentrations of carbon and oxygen. At the core of the BLING model is primary production with limitations by light, nitrate (NO_3), phosphate (PO_4), iron (Fe), and temperature, and subsequent remineralization of organic matter back to inorganic nutrients. Our version includes three phytoplankton types: large (B_{lg}), small (B_{sm}), and diazotrophs (B_{dia}). Small cells represent calcifying organisms; they use calcium carbonate to form shells. Diazotrophs have the ability to fix nitrogen so they are not limited by the availability of nitrate. Phytoplankton loss is expressed as a power law with a size-dependent exponent based on *Dunne et al*. [2005]. The evolution of biomass in each population is calculated as

$$\frac{\partial B_{lg}}{\partial t}=\left[\mu_0\, L_I \min\left(L_{NO_3}, L_{PO_4}, L_{Fe}\right)-\lambda_0\left(\frac{B_{lg}}{B_0}\right)^3\right]e^{\kappa T}\, B_{lg} \tag{1}$$

$$\frac{\partial B_{sm}}{\partial t}=\left[\mu_0\, L_I \min\left(L_{NO_3}, L_{PO_4}, L_{Fe}\right)-\lambda_0\left(\frac{B_{sm}}{B_0}\right)\right]e^{\kappa T}\, B_{sm} \tag{2}$$

$$\frac{\partial B_{\mathrm{dia}}}{\partial t}=\left[\mu_{0\mathrm{d}}\,L_{I}\min\left(L_{\mathrm{PO_4}},L_{\mathrm{Fe}}H(T-14)\right)-\lambda_0\left(\frac{B_{\mathrm{dia}}}{B_0}\right)\right]e^{\kappa_d T}\,B_{\mathrm{dia}} \tag{3}$$

where μ_0 and $\mu_{0\mathrm{d}}$ are the maximum photosynthesis rates; L_{I}, $L_{\mathrm{NO_3}}$, $L_{\mathrm{PO_4}}$, and L_{Fe} are functions describing limitation by light, nitrate, phosphate, and iron, respectively; λ_0, B_0, κ, and κ_{d} are constants, and T is temperature. A Heaviside function (*H*) inhibits diazotroph growth at temperatures below 14°C to prevent unrealistically large blooms at high latitudes. The density dependence of the population growth rate requires knowledge of the biomasses at a given time; these values are saved in the model but not advected or diffused by the flow. Initial phytoplankton abundances are prescribed, and the concentration of chlorophyll (chl) is diagnosed at each time step from the total biomass and the variable chlorophyll-to-carbon ratio.

Organic matter is distributed among three pools: a fraction becomes dissolved organic nitrogen and phosphorus (DON, DOP), a fraction is instantaneously recycled through the microbial loop in the euphotic zone, and the remaining fraction sinks as particulate organic matter and is instantaneously remineralized deeper in the water column. The fraction of sinking particles depends on phytoplankton size [*Dunne et al*., 2005; *Galbraith et al*., 2010]. DON and DOP are remineralized at constant rates.

Nitrogen cycling includes N_2 fixation by diazotrophs as well as benthic and pelagic denitrification, following the representation in the more complex GFDL-TOPAZ model of *Dunne et al*. [2013]. Iron chemistry includes organic and inorganic scavenging, a sediment source, and aeolian deposition of soluble iron from the climatology of *Mahowald et al*. [2005]. Flexible N:P and Fe:N stoichiometry are implemented.

There are numerous inputs required by the biogeochemical model. Parameters were manually tuned and are given in Table 1. Initial and boundary conditions for the biogeochemical tracers are constructed from a combination of climatologies and model output: the gridded Global Data Product version 2 (GLODAPv2) [*Key et al*., 2015; *Lauvset et al*., 2016] for DIC and alkalinity, the World Ocean Atlas 2013 (WOA13) for O_2, NO_3, and PO_4 [*Garcia et al*., 2014a,2014b], and a coarse resolution coupled global model with BLING simulation for Fe, DON, and DOP. Initial conditions are obtained after a 3 year spin-up. During the spin-up, DIC between 70°S and 30°S increases by an average of 23 μmol/kg in the top 100 m. This drift is partly due to the observed increase in the Southern Ocean carbon reservoir and the fact that the GLODAPv2 gridded product is normalized for the year 2002 [*Lauvset et al*., 2016]. In the top 100 m, alkalinity increases by 8 μmol/kg; nitrate and phosphate increase by 1.5 and 0.080 μmol/kg, respectively, and iron increases by 5×10^{-5} μmol/kg. Oxygen has a negative drift of -1.4 μmol/kg in the top 30 m, and a positive drift of 3.5 μmol/kg between 30 and 250 m. Drifts typically decrease with depth and are negligible below 1000 m. Initial conditions are then adjusted using the adjoint method, as described below.

2.3. Data Assimilation

This work is based on the software developed by the ECCO project, and a description of the method including the underlying equations can be found in *Stammer et al*. [2002] and *Wunsch and Heimbach* [2007]. Here we provide a general description of the 4D-Var optimization method. The overall goal is minimizing a cost function, $\mathcal{J}$, which is a sum of weighted squared model-data differences and weighted distances from the prior inputs. Prior inputs of the model to be optimized are referred to as "controls." In our case, the controls consist of initial conditions and surface boundary (atmospheric state) conditions.

The observations used for assimilation are referred to as "constraints." Our assimilation includes both physical and biogeochemical constraints (see Table 2 and section 2.4). The optimization goal is to have the model solution fit each observation within the uncertainty assigned. Uncertainties include measurement error as well as model representation error, which accounts for processes that are not expected to be correctly reproduced by the model, such as internal waves. Assigning proper uncertainties is key to the success of the adjoint method; data with smaller uncertainty will be stronger constraints for the optimization. The magnitude of the controls also contributes to the cost function; uncertainties are assigned to the model distance from the prior inputs. The total cost function is expressed as

$$\mathcal{J}=\sum_i\left(\mathrm{model}_i-\mathrm{obs}_i\right)^2\ \sigma_i{}^{-2}+\sum_j\Delta\mathrm{control}_j{}^2\ \sigma_j{}^{-2} \tag{4}$$

where "model$_i$" refers to the model value at the same time and location as the corresponding observation "obs$_i$", and Δcontrol$_j$ is the adjustment to the input parameter at a given time and location. Once controls

Table 2. Observational Constraints

Data Set	Variable(s)	Acquired From
Biogeochemical Observations		
bgc-Argo	O_2	http://runt.ocean.washington.edu/o2/
GLODAPv2	DIC, ALK, pH, O_2, NO_3, PO_4	http://cdiac.ornl.gov/oceans/GLODAPv2/
SOCATv4	pCO_2	http://cdiac.ornl.gov/ftp/oceans/SOCATv4/
Hydrographic Observations		
Argo	T, S	http://www.usgodae.org/
CTD	T, S	http://cchdo.ucsd.edu/
Seals	T, S	http://www.meop.net/
XBT	T	http://www-hrx.ucsd.edu/
Satellite Observations		
RADS	SSH	http://rads.tudelft.nl/rads/index.shtml
AVISO	Mean dynamic topography	http://www.aviso.altimetry.fr
Remote Sensing Systems Inc.	SST	http://www.remss.com/
NSDIC	Ice concentration	https://nsidc.org/data/seaice_index/

are determined that minimize the model misfit to the constraints, the state estimate is a produced as a free-running forward model simulation with closed budgets using the optimized inputs.

The dimensionality of the problem makes directly solving for the controls that minimize $\mathcal{J}$ impossible. Optimization is achieved via an iterative process. Success requires the utilization of the adjoint model, which solves for the gradient of the cost function with respect to all the controls in one calculation. At each location and time where a constraint is present, the adjoint model is "forced," with each constraint forcing's influence being relative to its contribution to $\mathcal{J}$. This adjoint model forcing is then propagated backward in time via the governing model equations to quantify how the perturbation manifests on all model inputs earlier in time. Thus the constraints comprise the input "forcing" on the adjoint model, and the adjoint output is the projection of all constraints on the gradient of $\mathcal{J}$ with respect to the controls. This gradient information is then used in the quasi-Newton search algorithm of *Nocedal* [1980] and *Gilbert and Lemaréchal* [1989] to minimize $\mathcal{J}$.

The numerics of the adjoint model are determined from the linearized governing equations of the "forward" MITgcm. Though the adjoint model is linear, it is time-stepped using the *temporally varying forward model state*, minimizing errors due to the linear approximation. These errors can still be significant, however, especially for long assimilation windows. A primary example occurs when the model state nears baroclinic instability. The adjoint model may calculate a strong sensitivity to the controls that can trigger the instability at this time step. The linear adjoint cannot, however, determine that triggering the instability would then release available potential energy. Thus, at the next time step, the adjoint model again accumulates sensitivity to the controls that can trigger the instability, and this can lead to exponential growth of the adjoint-determined gradients. A key to success is running the adjoint model with enhanced viscosity to damp out these exponentially growing sensitivities. We want to realize the sensitivity, but also damp it out before it overwhelms the solution. The viscosity in the adjoint model for this work is 10 times larger than in the forward model. Because of the enhanced viscosity and linearization approximation, the adjoint-determined gradients are not *exact* gradients, but they are accurate enough to allow us to optimize the model solution. We elaborate on the accuracy of the adjoint-derived gradients in section 3.

Even with accurate adjoint gradients, the model may not be brought into consistency with all constraints due to model error limiting controllability of the solution. With a perfect model and inputs, one would be able to reproduce the Southern Ocean state. However, given model errors, even with perfect inputs the solution would drift from the true state. Some aspects of the solution, for example, reproducing the meandering of the Antarctic Circumpolar Current, may be poorly captured. One may remedy this by reducing model errors, or by breaking the dynamical budgets via sequential optimization. We have chosen to keep the dynamical budgets closed to increase scientific value of B-SOSE at the expense of consistency with observations.

With the implementation of biogeochemical constraints, it is worth noting that the 4D-Var method can, in theory, handle a vector of constraints of any dimension and being over-constrained or under-constrained is not a technical problem. The adjoint is linear, and the constraint "forcings" on the adjoint model add influence independent of the other constraints or the current adjoint state. If there are two observations in the same location at the same time, their impact is added linearly to the sensitivities. If consistent with each other, they add to a stronger forcing; if inconsistent they compensate each other. Thus if there is a pCO_2 measurement in SOCATv4 co-occurring with DIC and alkalinity measurements in GLODAPv2, they will all be used as constraints. Similarly, satellite SST observations and Argo temperature profiles can co-occur and both will be used. There are no technical obstacles to using co-located or redundant data as constraints.

2.4. Observational Constraints and Their Uncertainties

Biogeochemical constraints, listed in Table 2, include in situ observations of the carbon system, oxygen, and nutrients in the Southern Ocean during the period 2008–2012. Data are obtained from the following data sets: calibrated oxygen profiles from bgc-Argo (http://runt.ocean.washington.edu/o2/), the GLODAPv2 in situ data product [*Key et al.*, 2015; *Olsen et al.*, 2016], and the Surface Ocean CO_2 product version 4 (SOCATv4) [*Bakker et al.*, 2016]. Chlorophyll data from in situ measurements and derived from satellite observations of ocean color are not used at this time, though we expect to implement these constraints into a future version of B-SOSE.

Uncertainties on the biogeochemical constraints are estimated as the sum of measurement error and model representation error. The measurement uncertainty accounts for factors such as instrument error, data calibration, standardization, and interlaboratory differences. We use the following values: 2 μmol/kg for DIC, 4 μmol/kg for alkalinity, 1 μmol/kg for O_2, 0.01 for pH, and 1 μatm for pCO_2; for nutrients, we assume 2% of the spatially varying mean concentration. Model representational error is the part of the ocean variability that cannot be reproduced by the model or corrected by optimization. Ideally, representation error would be estimated by comparing the evolution of modeled fields to observations, but since we lack sufficient observational coverage for this type of assessment, we rely on the statistics of model solutions to infer the model error. For our first guess, we assign the error to be 0.7 times the standard deviation of each biogeochemical field using monthly averaged output from a 130 year forward simulation derived using the same setup described in this manuscript but with looped 2005 to 2014 forcing. The result is a three-dimensional error that generally decreases with depth because the variability is higher near the surface; dynamically complex regions also have larger error. Values at different depth levels are summarized in Table 3. Future work will refine this estimate of model representation error.

Other constraints include observations from the Jason 1 and 2 altimeters acquired from the Radar Altimetry Database System (RADS) and a mean dynamic topography, MDT_CNES-CLS13. A daily sea surface temperature product is derived from microwave radiometers and optimally interpolated (OI MW SST) by Remote Sensing Systems Inc. Ice concentration observations from the National Snow and Ice Data Center (NSIDC) [*Meier et al.*, 2013, updated 2016] are used. All available temperature and salinity measurements from Argo float profiles, conductivity-temperature-depth (CTD) synoptic sections, instrumented seals and expendable bathythermographs (XBT) are used to constrain the solution. Links to the data sources are listed in Table 2.

Uncertainties for the physical variables are derived as follows. For temperature and salinity, the Argo observation misfits to the climatology by *Roemmich and Gilson* [2009] are calculated and then objectively mapped. Thus, the model is constrained to be as consistent with Argo profiles as the climatology. This is a rather stringent constraint as it does not include the formal mapping error from the climatology, and thus

Table 3. Model Representation Error (South of 30°S) for Biogeochemical Properties

	Surface		200 m		1000 m		
Field	Mean	Std. dev.	Mean	Std. dev.	Mean	Std. dev.	Max
DIC (μmol/kg)	5.9	2.4	4.3	1.9	2.3	1.6	18.7
Alk (μmol/kg)	5.1	2.5	2.7	1.4	1.6	0.93	25.8
O_2 (μmol/kg)	3.4	1.0	7.3	3.9	2.3	1.4	27.5
NO_3 (μmol/kg)	0.73	0.27	0.69	0.27	0.29	0.13	2.7
PO_4 (μmol/kg)	0.049	0.016	0.047	0.017	0.018	0.0077	0.18
Fe (μmol/kg)	1.7×10^{-5}	8.2×10^{-6}	2.5×10^{-5}	1.1×10^{-5}	7.5×10^{-6}	5.9×10^{-6}	1.2×10^{-4}
pH (–)	0.0079	0.0029	0.012	0.0039	0.0086	0.0024	0.041
pCO_2 (μatm)	7.3	2.3					21.6

in under-sampled regions we risk over-constraining the model. We do, however, choose a minimum uncertainty of 0.05°C and 0.005 g/kg. The temperature uncertainty at 2 m is used to constrain the OI MW SST product, but increased by a factor of 10 as all the OI MW SST values used are not independent. We constrain to capture 95% of the variance of the SSH signal from the Jason 1 and 2 altimeters, $\sigma_{SSH} = \sqrt{\mathrm{var}(SSH_{obs}) \times 0.05}$. Due to complications with the sea ice model adjoint, the ice is constrained by penalizing sea surface temperature, by requiring the ocean to be colder where ice cover is deficient and warmer where ice cover is excessive.

Model error dominates over measurement error for most data assimilated in B-SOSE. This means that observations coming from multiple sources, such as O_2 constraints from Argo and GLODAPv2, will be assigned similar weights that reflect primarily the location of those observations. For the case of surface temperature from Argo and satellite radiometers, however, the measurement error in the satellite product is significant and contributes to the uncertainty in a nonnegligible way.

2.5. Control Variables and Their Uncertainties

The model controls adjusted through the adjoint method are atmospheric temperature, specific humidity, shortwave and longwave downwelling radiation, precipitation, meridional and zonal wind speeds, as well as initial conditions of temperature, salinity, DIC, alkalinity, O_2, NO_3, PO_4, and Fe. Adjustments to those fields are limited by imposing a penalty that is the weighted distance from the products to which they are constrained. Atmospheric state fields are constrained to ERA-Interim [*Dee et al.*, 2011]. Temperature and salinity are constrained to a hybrid product informed from ECCOv4 and SOSE. Biogeochemical tracers are constrained to the products used to produce their initial conditions: GLODAPv2 for DIC and alkalinity, WOA13 for O_2, NO_3, and PO_4, and the global BLING model output for Fe. To determine consistency of the controls with the constraining product, the uncertainty must be prescribed. Below we describe the method used to estimate this uncertainty.

For biogeochemical initial conditions, the uncertainty is proportional to the standard deviation of each tracer in the forward simulation; it is equal to the model representation error described in the previous subsection, with values summarized in Table 3. Uncertainty for temperature and salinity initial conditions is proportional to the Argo residuals to the *Roemmich and Gilson* [2009] climatology derived as explained in the previous subsection. Uncertainty is increased from this estimate by a factor of 10 poleward of 30°S, but reduced equatorward of 30°S as our focus is not to constrain or cause much changes to the controls in the subtropics and tropics. The uncertainty on the prescribed atmospheric state is taken to be the standard deviation of the ERA-Interim fields between 2004 and 2014. While this is likely an overestimate of the uncertainty, we find the control magnitudes to be reasonable. For example, a typical perturbation to the ERA-Interim 2 m temperature is about 1°C. Control variables are provided and plotted at sose.ucsd.edu. The model diffusion operator is used to enforce spatial correlation scales on the controls. An isotropic smoothness scale of 60 km is enforced for the atmospheric controls. Adjusted initial conditions are smoothed using a scale of 20 km in the horizontal and 10 m in the vertical.

3. Verification of the Adjoint Model

The adjoint model yields the gradients, or partial derivatives, of a cost function with respect to model state and model inputs. One validates the adjoint model using a "gradient check," which compares the adjoint-derived gradients with the sensitivities calculated from the change in cost resulting from small perturbations in the forward model. Infinitesimal perturbations to the forward model are unlikely to drive strong nonlinearities and, assuming the adjoint code is correct, will perfectly match the change in the cost function predicted from the adjoint-derived gradient. Here we check the accuracy of the adjoint for the practical case of biogeochemical state estimation by using perturbations that are of a magnitude representative of an actual adjustment to the controls (in this case 1% of the climatological value). Furthermore, we choose to test the adjoint model in Drake Passage, which is a region of high eddy kinetic energy. Thus our gradient checks test both the adjoint code and the validity of the linearity approximation for our setup.

For the sensitivity experiments, a cost function must be defined that represents the quantity for which one wishes to derive the gradient with respect to other model fields at earlier times. Instead of the model-observations misfit cost function used for data assimilation, we choose variables on a section along Drake

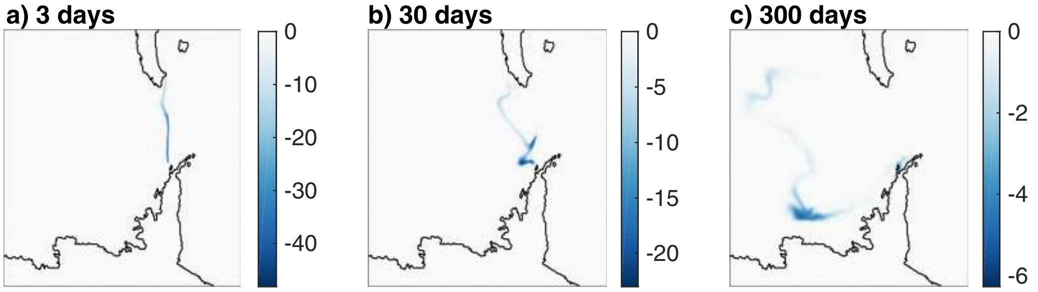

Figure 3. Depth-integrated sensitivity of the pH cost function to DIC after 3, 30, and 300 days of adjoint integration. Units are (μmol C/kg)$^{-1}$ m.

Passage (longitude 295.2°E) on 1 February 2009 to be the quantity of interest. A localized cost function allows tracking the propagation of sensitivities backward in time (Figure 3). We test two variables: upper ocean pH (50–100 m depth) and interior oxygen (200–300 m depth). The cost is defined as the square of model fields (pH or oxygen) integrated over a period of time (from midnight on 1 February 2009 to midnight on 2 February 2009) and over latitude and depth (within the range mentioned above).

The adjoint sensitivity is the projected change in cost resulting from a unit perturbation of one control variable at a single point in space and in time. The sensitivity of the pH cost function to DIC is shown in Figure 3. At each location, the vertically integrated sensitivity is plotted. Three snapshots are shown, giving the sensitivity to DIC on 29 January, 2 January, and 7 April (3, 30, and 300 days earlier, respectively). Negative values indicate that an increase in DIC will cause pH to go down, as expected. We can see that the sensitivities fade and move upstream as we go back in time.

For each time (3, 30, and 300 days), we select one location where the sensitivity is large to test the gradients. For example, the adjoint sensitivity of the pH cost function to DIC at 75 m, 291.2°E, 64°S on 29 January is -321.3058. We then run the forward model twice, once increasing DIC by 1% and once reducing it by 1% at that time and location. The forward model sensitivity is given by

$$\mathrm{FWD}=\frac{\mathrm{cost}(+)-\mathrm{cost}(-)}{\Delta\mathrm{DIC}(+)-\Delta\mathrm{DIC}(-)}, \tag{5}$$

where ΔDIC is the magnitude of the perturbation and $(+)$ and $(-)$ refer to the positive and negative perturbations. The error in the adjoint-derived gradient is

$$\mathrm{error}=\frac{\mathrm{ADJ}-\mathrm{FWD}}{\mathrm{FWD}}, \tag{6}$$

where ADJ is the adjoint sensitivity. For this experiment, the forward model sensitivity is -321.1217, yielding an error of 0.057%. In addition, we examined the sensitivity to iron and temperature. The results are summarized in Figure 4a. We repeat the procedure for the oxygen cost function, replacing DIC perturbations with oxygen perturbations (Figure 4b).

The adjoint of the coupled biogeochemical-sea ice-ocean model passes the gradient check, indicating that the adjoint model has been successfully derived. The errors are small, typically much less than 1%, for timescales of 3–30 days. An exception is the sensitivity of pH to temperature, which is around 2%. Errors reach 20% for 300 day long adjoint runs for DIC with respect to pH changes and for temperature with respect to both pH and oxygen changes. Errors in the other gradients are approximately 1% even after 300 days. As expected, the errors tend to increase with adjoint integration length since the chance of nonlinear events, such as convection, affecting the solution, and temperature in particular, increases on longer timescales. A monotonic increase in error with time is not found, however, likely due to the fact that for practical reasons we only tested a single location as opposed to an ensemble of locations.

Figure 3c shows that the adjoint model predicts perturbations to upper ocean pH in Drake Passage covary with DIC concentration off Thurston Island in the Amundsen Sea 300 days earlier. Forward model perturbation experiments confirmed this covariance to have an error of approximately 20%. This error magnitude is rather insignificant when one considers the iterative procedure taken to find the cost function minimum.

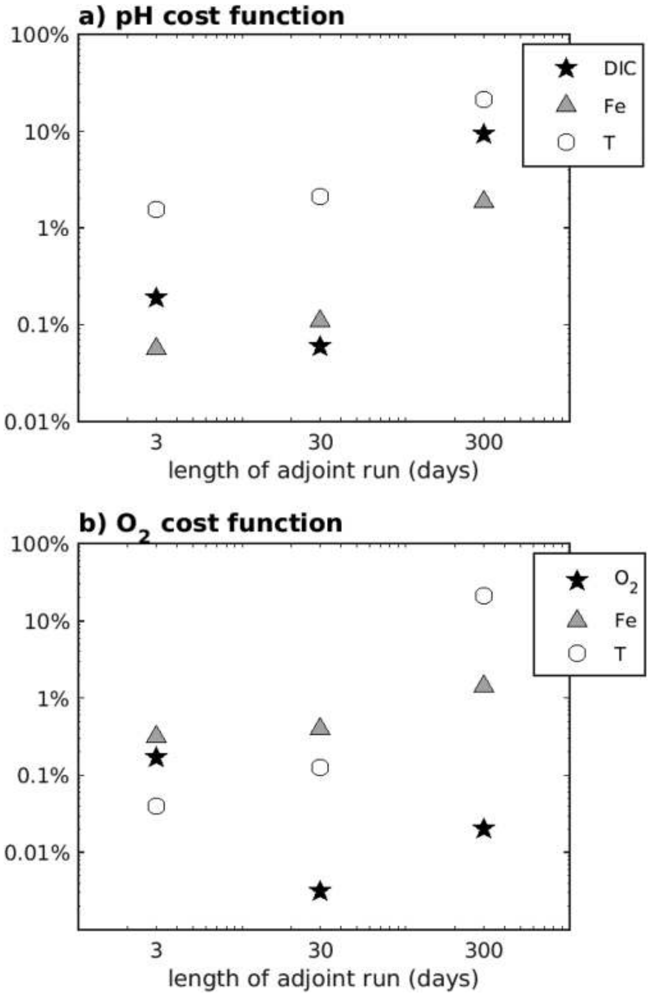

Figure 4. Error in adjoint sensitivities relative to the true sensitivities from finite difference perturbation experiments. (top) pH cost and (bottom) O_2 cost. We compare the change in cost per unit change in control variable to the partial derivatives yielded by the adjoint for adjoint integration periods ranging from 3 to 300 days.

Thus, the accuracy even over long integrations of 300 days gives confidence that the adjoint model is able to adequately quantify the full space-time covariance and propagate the constraint information throughout the domain and across variables. This gradient information allows iteratively solving for the control vector to produce a state estimate. Here we have shown the accuracy of adjoint gradients in the Drake Passage; additional experiments have confirmed the agreement of adjoint and forward sensitivities in other locations throughout the Southern Ocean (not shown). In the end, the practical test for the adjoint model is the ability to bring down a cost function, such as the weighed model-observations misfits for production of a state estimate.

4. State Estimate 2008–2012

The adjoint model, which was shown in the previous section to accurately propagate constraint information, is used to produce an estimate of the physical and biogeochemical state of the Southern Ocean for the years 2008–2012. The product, available online at http://sose_ucsd.edu/bsose_results.html, is the result of 105 iterations of the optimization method. With each iteration, the cost function (a weighed model-observation misfit) becomes smaller, indicating that the solution becomes more consistent with the data. We publish iteration 105 as the state estimate because the iterative cost reduction was becoming negligible. For example, iteration 105 cost was only 2% less than iteration 104 and the cost for iteration 106 was slightly larger than iteration 105. With great effort the solution could be made more consistent with the observations. However, as demonstrated below, the consistency of the iteration 105 solution with the observations was deemed adequate, making this state estimate worthy of publication and analysis.

Before 4D-Var optimization can be employed, a prior model solution must be attained. Numerous model runs were carried out to manually optimize parameterizations and produce a prior model run, iteration 0, which uses the default controls specified in section 2.5. For the atmospheric forcing, this means the ERA-Interim analyzed fields without adjustment. In Figure 5, we see that the normalized cost associated with each biogeochemical data set has been reduced in the state estimate compared to the prior. The costs for the controls and physical constraints are not shown. A normalized cost value of 1 means that the fit to the data is within the prescribed uncertainty. While we have not achieved that level of consistency, it is clear that data assimilation brought the solution closer to the observations. Oxygen observations have the largest normalized cost of all assimilated data, suggesting that the model representation error assigned may be too small in some regions. There are 2148 GLODAPv2 profiles and 8905 Argo profiles with oxygen data

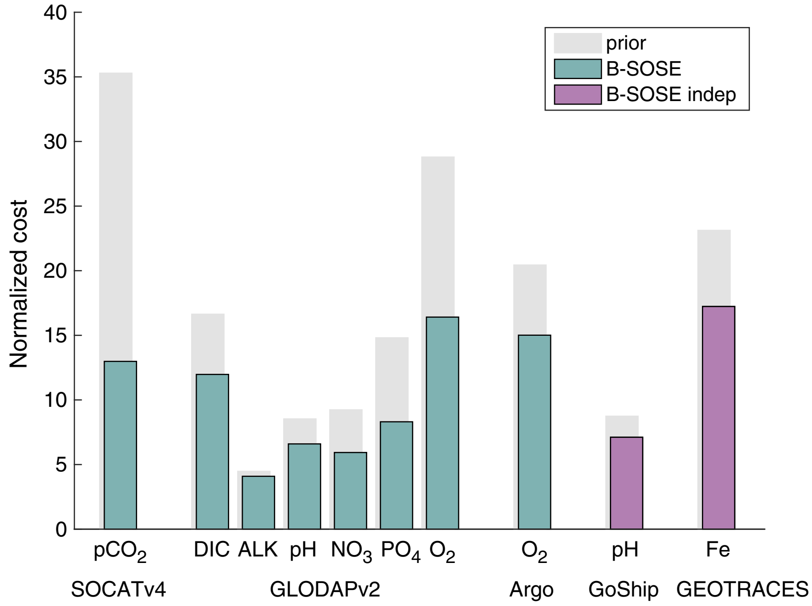

Figure 5. Normalized cost for each data set in the "prior," forward model run (gray bars) and in the state estimate (colored bars) which is constrained to the SOCATv4, GLODAPv2, and Argo data sets. Underway pH data from a Go-Ship cruise and iron concentrations from the GEOTRACESv3 data set are not assimilated and thus provide an independent data set against which the state estimate can be validated. A normalized cost value of 1 means that the fit to the data is within the prescribed uncertainty.

during our assimilation window. In the prior run, the normalized cost is higher for GLODAPv2 constraints; the adjoint brings the costs for both data sets to a similar level.

Near surface observations are more readily fit as the optimization has more control on properties directly interacting with the atmospheric state. As such, it is unsurprising that the largest cost reduction for the biogeochemical constraints is for the surface pCO_2 SOCATv4 data set. Even with model error, if there were no other constraints we could likely bring the solution into complete consistency with observed pCO_2 by changing the local surface temperature through controls on the surface heat fluxes. This could, however, introduce inconsistencies with the other constraints, such as surface temperature, sea surface height, DIC, or oxygen observations. The requirement of simultaneously fitting multiple constraints and the presence of model error may prevent the optimization from being brought into consistency with all data.

Though it is not guaranteed that the solution will be consistent with all assimilated data, it is still useful to compare to independent data sets. These comparisons validate the skill of the optimization method to propagate observational constraint information. One data sets that was not assimilated is the underway pH data from GO-SHIP

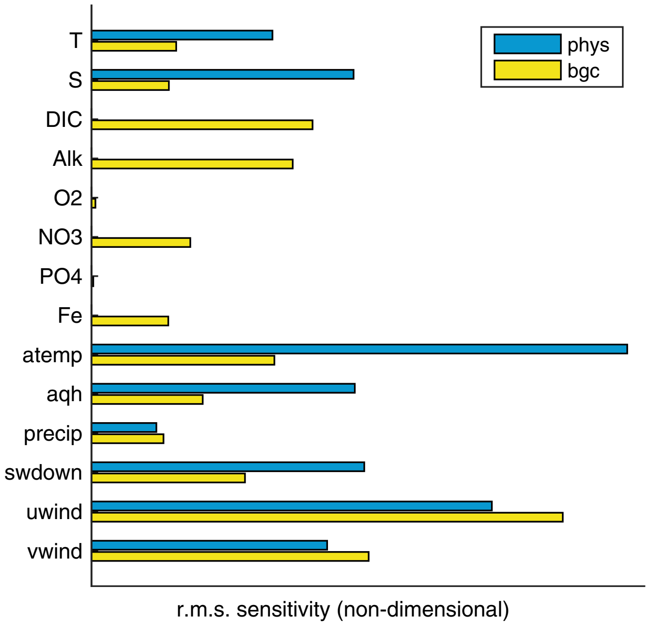

Figure 6. Sensitivity to the B-SOSE controls for the physical constraints (blue) and biogeochemical constraints (yellow) during 2008 in the prior run. Sensitivities are normalized by the uncertainty on each control and the root mean square (r.m.s.) is plotted. Controls are: initial conditions for potential temperature, salinity, and six biogeochemical tracers (DIC, alkalinity, oxygen, nitrate, phosphate, and iron) as well as time-varying atmospheric state (surface air temperature, surface air humidity, precipitation, shortwave downwelling radiation, zonal wind speed, and meridional wind speed).

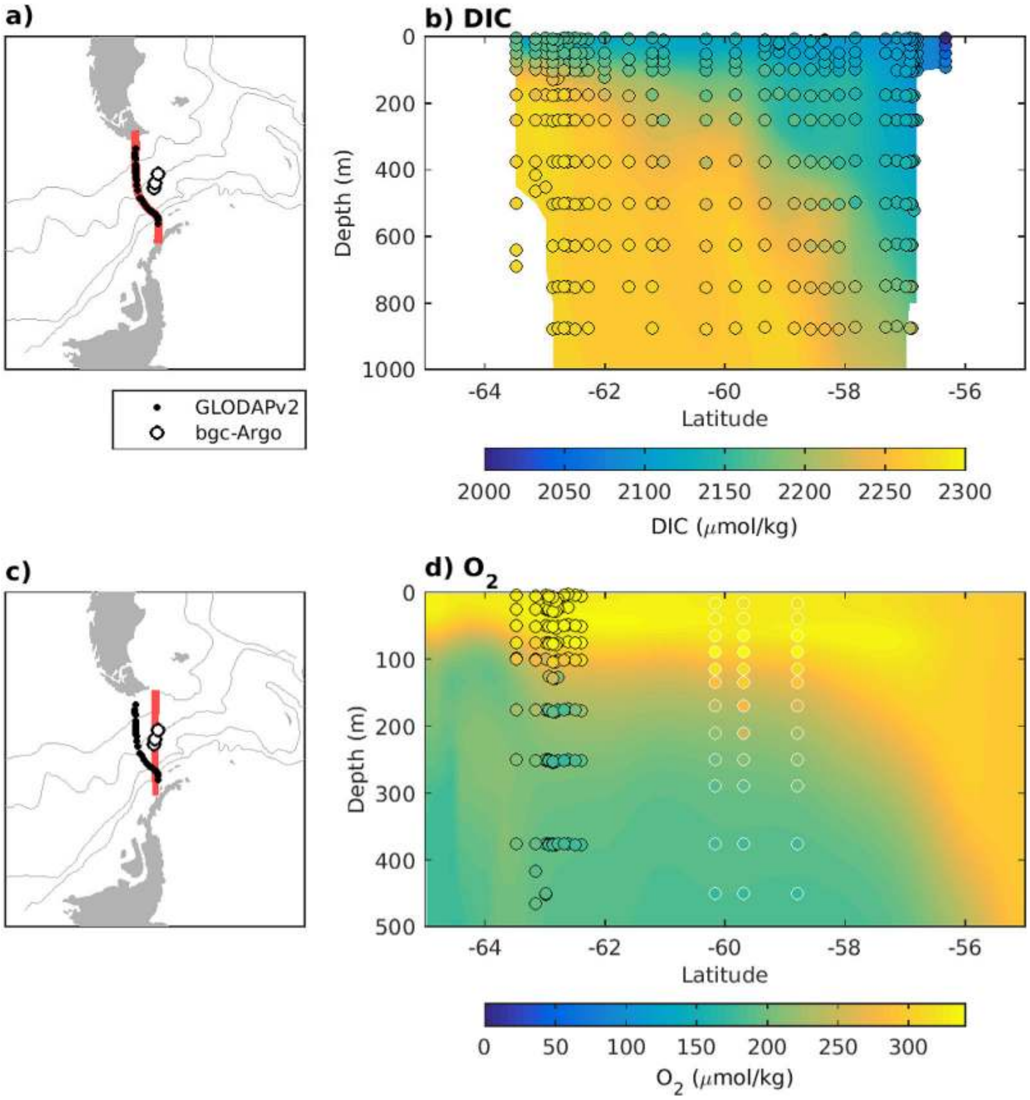

Figure 7. Model-data comparisons for (a, b) DIC and (c, d) oxygen in February 2009. Observations are shown as colored bubbles, modeled fields as background shading. Three bgc-Argo profiles (white contoured bubbles) were taken nearby a GLODAPv2 section (black contoured bubbles) across Drake Passage in February 2009 [*Bakker et al*., 2013], whereas O_2 is averaged between 63°W and 65°W (red curves in plots a and c).

A13.5 occupied in 2010 [*Bullister et al*., 2010]. Another is the iron concentration observations compiled in GEOTRACESv3 [*Mawji et al*., 2015]. Both independent data sets are better fit by the state estimate than by the prior solution, indicating that data assimilation has improved the estimate of the biogeochemical state of the Southern Ocean.

The change in cost is due in part to the assimilation of biogeochemical data, and in part to the assimilation of physical data. Temperature, salinity, and sea surface height observations constrain the circulation and solubility, giving them a strong impact on biogeochemical properties. Meanwhile biogeochemical properties often have strong vertical gradients, allowing them to significantly constrain the circulation and vertical exchanges. To quantify the relative influence of each type of constraint, we examine how sensitive the prior misfits are to the control parameters. We perform two experiments, one in which the cost function consists of only physical constraints and another in which it consists of only biogeochemical constraints (Figure 6). Both are run for 1 year (2008) in the prior setup (in order to avoid adjustments to the controls being part of the cost function). The larger the sensitivity, the more influence the constraints have on the optimization. For the 2008–2012 B-SOSE, the physical cost has a greater impact than the biogeochemical cost with respect to all physical constraints except winds and precipitation, but the magnitudes are comparable. In our setup, the physical cost has no sensitivity to biogeochemical controls because the biology does not feedback on the physical state. The relative influence of the biogeochemical constraints compared to the physical constraints ranges from 30% to 118%. Thus biogeochemical observations have a significant impact on the coupled state estimate.

One expects significant uncertainty in estimates of the upper ocean carbon cycle due to the complex dynamics occurring over a large range of space and timescales. B-SOSE has an idealized representation of biological activity and there is a significant lack of constraints from any one source. Therefore, B-SOSE assimilates the observing system as a whole to maximize our knowledge. With regards to biogeochemical constraints for the 2008–2012 period, the best in situ coverage comes from the SOCATv4 data set, which provides extensive coverage but only constrains the surface properties, and from Argo floats equipped with oxygen sensors. The GLODAPv2 data set provides valuable observations of the carbon system and nutrients; however, these sparse observations are concentrated in austral summer. The biogeochemical and physical constraints are able to provide confidence in the B-SOSE representation of the seasonal to interannual variability below the ocean mixed layer. Nevertheless, in what follows we evaluate B-SOSE at all depths due to the importance of upper ocean processes to the climate system.

We first visualize the qualitative agreement between the state estimate and observations by plotting observed profiles over simulated fields along a section in the Southern Ocean. In February 2009, there were three bgc-Argo profiles located near a repeat hydrographic section (WOCE section SR1) [*Bakker et al.*, 2013], which starts at approximately 69°W, 56°S and ends at 63°W, 64°S (Figure 7a). In Figure 7b, we show DIC observations overlain on the modeled DIC along this line averaged over the month of February 2009. Observations are shown as colored dots, with black contours for GLODAPv2. In Figure 7d, a similar plot shows simulated oxygen averaged in February 2009 between 63°W and 65°W. Observations are shown as colored dots, with black contours for GLODAPv2 and white contours for bgc-Argo. It is clear from Figure 7 that the state estimate broadly captures the latitudinal gradients in DIC and oxygen as well as their vertical profiles.

It is crucial to quantify the overall statistics of the model-data differences. However, the dimensionality of the disparate constraints makes it difficult to summarize the agreement of the state estimate with all individual profiles. To help visualize the model-observation misfits statistics, we have developed a semiautomated methodology for creating a suite of figures that show aspects of the misfits for each data set. The procedure includes binning misfits in time and space, then plotting the mean and standard deviation of the misfits on selected depth levels, zonal or meridional sections, or as a function of time, latitude, longitude, or depth. In addition, comparisons of the state estimate with climatologies are produced. For biogeochemical fields, we use climatologies from WOA13 [*Garcia et al.*, 2014a,2014b], the GLODAPv2 gridded product [*Key et al.*, 2015; *Lauvset et al.*, 2016], and the SOCATv4 gridded product [*Bakker et al.*, 2016]. These validation plots are available at http://sose.ucsd.edu/bsose_valid.html.

As an example of the type of validation diagnostics being generated, the misfits with bgc-Argo oxygen data are plotted as a function of latitude at two depth levels, 200 and 1000 m (Figure 8). In addition to model-observations misfits (red curves), we also show the misfit between the WOA13 climatology [*Garcia et al.*, 2014a,2014b] and the observations (gray curves). The mean and standard deviation of the binned misfits are shown. At 200 m, mean misfits tend to be higher for the state estimate than for the climatology, especially in the subtropics. However, the standard deviation within the bin is lower for the state estimate, indicating that although the mean bias is larger in the model than in WOA13, the state estimate does well at capturing the observed scales of variability. At 1000 m, the skill of the state estimate is comparable to the skill of the climatology. If we consider all data south of 30°S (no binning), at 200 m the state estimate captures 63% of the variance, compared to 53% for the climatology. At 1000 m, the state estimate and climatology capture 62% and 59% of the variance, respectively.

As shown, analysis of the statistics of the model-data misfits reveals biases. Notable biases are that B-SOSE is too rich in oxygen at the surface in midlatitudes (Figure 8), and B-SOSE pCO_2 is biased high in the subtropics with respect to SOCATv4, especially during summer (not shown). Nevertheless, the state estimate is able to fit the observations with minimal biases in many regions. For example, the Drake Passage repeat line provides the only nearly continuous time series of pCO_2 in the Southern Ocean [*Munro et al.*, 2015a,2015b; *Bakker et al.*, 2016]. In Figure 9, we show the 1 month bin-averaged observations in the area

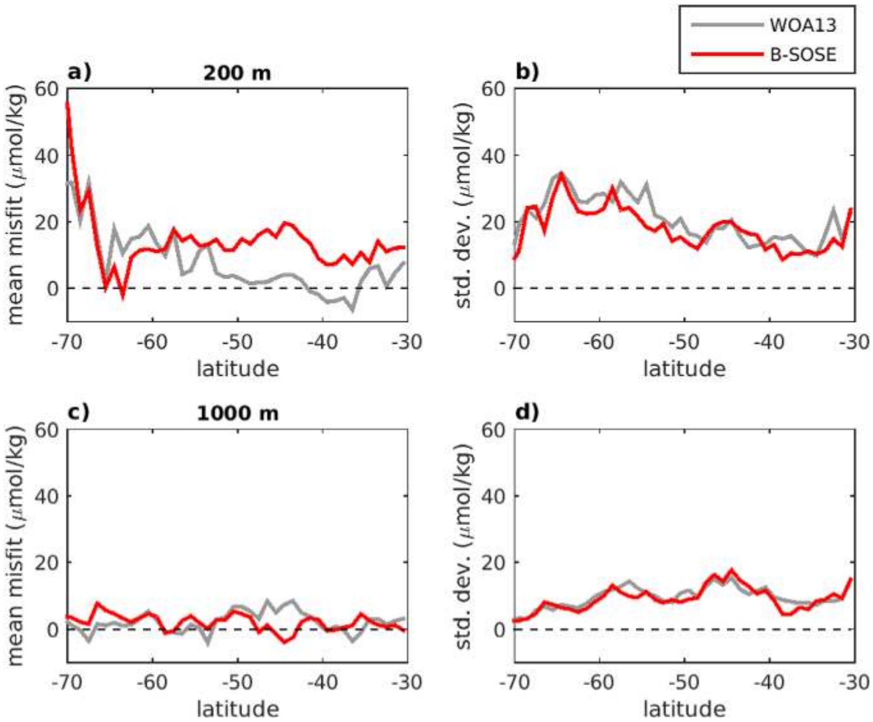

Figure 8. (left) Mean and (right) standard deviation of the misfit between bgc-Argo O_2 observations and the state estimate (red) and the misfit between observations and World Ocean Atlas 2013 climatology (gray). Misfits are binned in latitude (1 degree bins). Top row: 200 m and bottom row: 1000 m. The skill of the state estimate at fitting observations is comparable to the skill of the climatology product, with added benefits of high spatial and temporal resolution, consistent ocean dynamics, and closed budgets for biogeochemical tracers.

between 75°W and 55°W (black curve). The monthly averaged pCO_2 from the state estimate over the same area (pink curve) tends to be higher during the summer months. When the state estimate is subsampled at the time and location of the observations (red curve), the summer fit is improved, though the large drops in pCO_2 that occurred in 2009 and 2011 are still underestimated. For these comparisons, observations taken in regions shallower than 1000 m are excluded from the time series, as the B-SOSE solution is known to poorly capture coastal dynamics and biogeochemistry. Though the state estimate misses some of the extreme values in this time series, it is able to capture 37% of the variance of monthly averaged pCO_2.

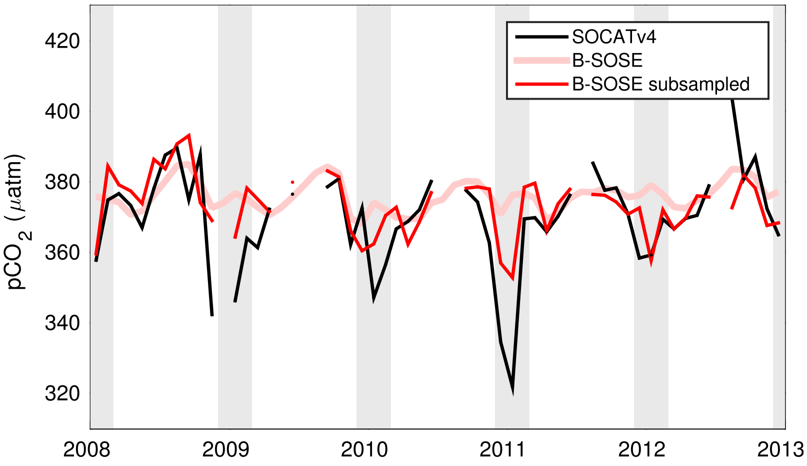

Figure 9. Monthly averaged pCO_2 in Drake Passage (75°W to 55°W, south of 50°S) from SOCATv4 observations (black) [*Bakker et al.*, 2016; *Munro et al.*, 2015a,2015b], from B-SOSE (pink), and from the B-SOSE solution subsampled at the location of SOCATv4 observations (red). Gray shading indicates summer months (December–February).

5. Utility of the State Estimate

5.1. Air-Sea CO_2 Flux

Diagnosing the B-SOSE CO_2 flux is useful as the extensive validation provided with the solution informs where this estimate may be trustworthy and where it may be biased. Furthermore, contrasting this new inference of air-sea carbon exchange with existing inferences helps inform the level of uncertainty in our knowledge. While the Southern Ocean is known to be a sink for anthropogenic carbon [e.g., *Khatiwala et al.*, 2009], there is an ongoing debate about whether the CO_2 uptake is increasing or slowing down [*Le Quéré et al.*, 2007; *Le Quéré*, 2010; *Le Quéré et al.*, 2010; *Metzl*, 2009; *Takahashi et al.*, 2009, 2012; *Lovenduski et al.*, 2013; *Khatiwala et al.*, 2013; *Fay et al.*, 2013; *Fay and McKinley*, 2014; *Majkut et al.*, 2014; *Landschützer et al.*, 2015; *Munro et al.*, 2015a; *McKinley et al.*, 2017]. Large interannual variability and sparsity of in situ data make detection of trends difficult [*Fay and McKinley*, 2014; *Lovenduski et al.*, 2015; *McKinley et al.*, 2017]. A

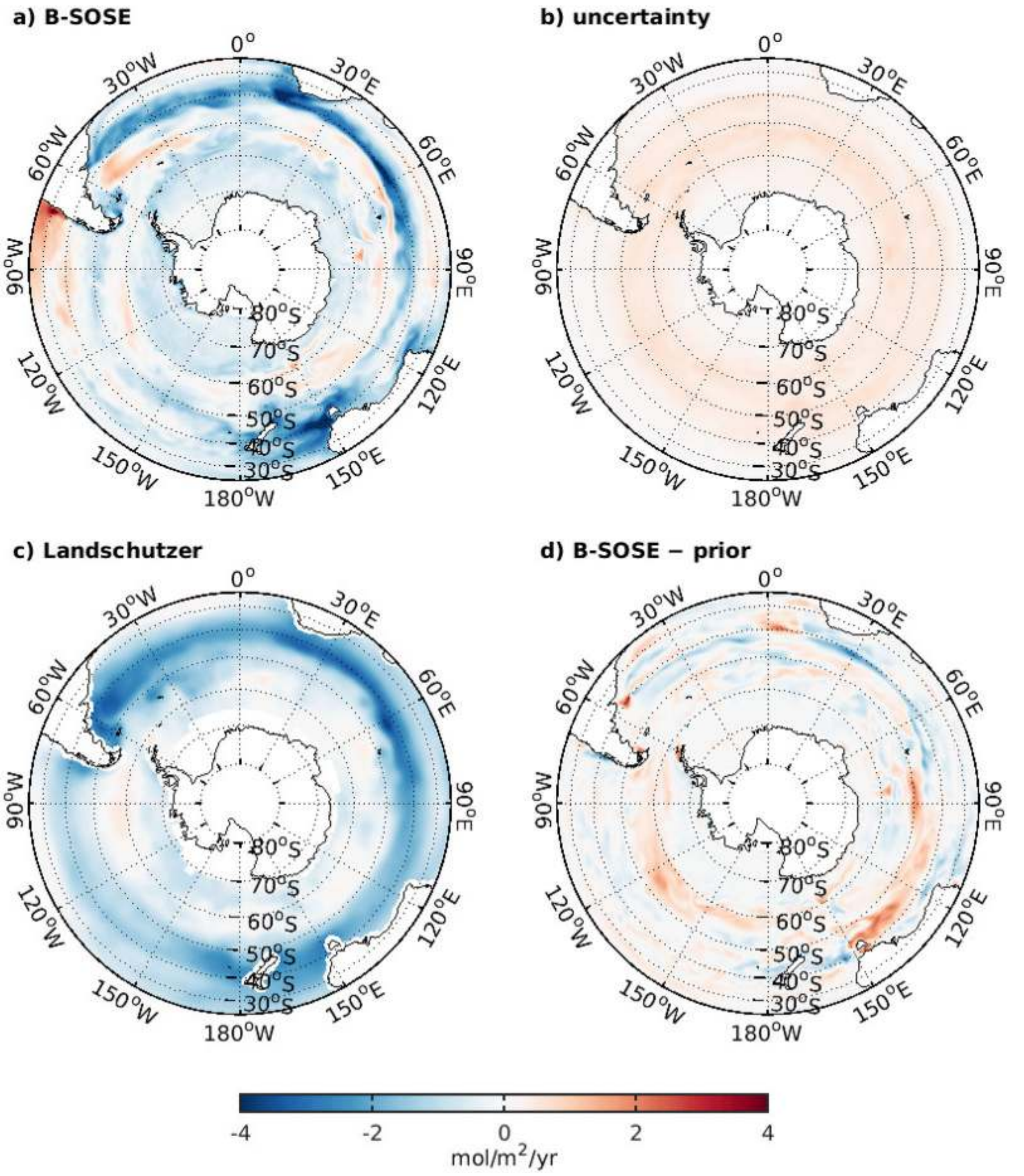

Figure 10. Mean air-sea flux of CO_2 for 2008–2011 (a) in the state estimate and (c) according to *Landschützer et al.* [2015]. Positive fluxes are into the atmosphere. (b) Uncertainty of the B-SOSE air-sea CO_2 flux estimated from a cost function sensitivity experiment (see text for details). The maximum value of the estimated uncertainty is 1.00. (d) Difference in air-sea CO_2 flux between the state estimate and the "prior," forward model run. Over 70% of the domain, the magnitude of the correction resulting from data assimilation exceeds the uncertainty estimate.

goal of B-SOSE is to provide a baseline in the form of a best estimate of the 2008–2012 Southern Ocean carbon system.

The B-SOSE mean CO_2 flux for 2008–2011 (Figure 10a) shows regions of strong biological carbon drawdown near topography and also in the subpolar gyres. Locations where upwelling leads to net outgassing are found in the Antarctic Circumpolar Current (ACC). The pattern agrees well with the estimate of *Landschützer et al*. [2015] for the same time period (Figure 10c). Note that the *Landschützer et al*. [2015] product ends in 2011, which is why we exclude 2012 from our average flux in Figure 10a. One discrepancy between the two products occurs in the Argentine basin (South Atlantic between 40°S and 50°S); net outgassing in the state estimate is likely the result of problems with the physical circulation, as large temperature and salinity misfits occur in that area. Outgassing at midlatitudes in the Indian Ocean and Eastern South Pacific occurs because the simulated net community production (NCP) is negative in those areas, as respiration of dissolved organic matter advected from lower latitudes exceeds local primary production. There are insufficient biogeochemical constraints to rule whether this is realistic or not, and it is possible that biological production is underestimated, which is one of many causes of uncertainty in the solution.

To quantify the uncertainty (Figure 10b), we use the fact that the cost is a measure of the log of the likelihood associated with a particular solution. We performed an ensemble of runs with perturbed model parameters. Each realization is given a weight which is a function of the misfit (cost) to SOCATv4 observations. The uncertainty is then calculated as the weighted standard deviation of simulated air-sea CO_2 fluxes. The parameters that were perturbed are vertical diffusivity, maximum photosynthesis rate, iron half-saturation concentration, and the temperature dependence of gas solubility. Each realization produces a different map of air-sea CO_2 fluxes, but if the cost is not much higher than the cost for the state estimate this other solution is only slightly less likely than the state estimate. Weights decrease proportionally to $\exp(-\sigma\,\mathrm{cost})$, where cost is the weighted misfit to SOCATv4 data and σ is chosen so that the weights become negligible when the cost is more than 10% higher than the cost for the state estimate. Since the pattern of estimated uncertainties shown in Figure 10b is fairly zonal, the root mean square is calculated at each latitude; the value is 0.19 mol/m^2/yr at 70°S and increases almost monotonically to a maximum value of 0.54 mol/m^2/yr at 53°S; there is second peak of 0.47 mol/m^2/yr around 40°S, then values decrease to 0.34 mol/m^2/yr at 30°S.

The effect of data assimilation on the solution is quantified by the change in air-sea CO_2 fluxes between the prior and the state estimate (Figure 10d). The result highlights that the magnitude of the change is on average larger than the uncertainty (over 70% of the domain), and thus that the impact of optimization is meaningful in constraining air-sea CO_2 fluxes.

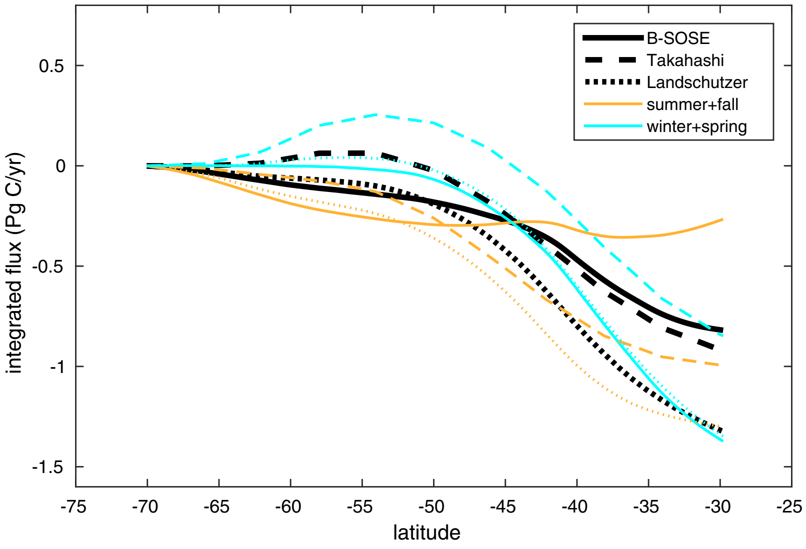

Figure 11. Integrated air-sea CO_2 flux. Fluxes are integrated from the South Pole to a given latitude (x axis). The B-SOSE estimate (solid curves) is compared to the *Landschützer et al.* [2015] (dotted curves) and *Takahashi et al.* [2009] (dashed curves) estimates. Annual mean values are shown in black, summer and fall averages in orange, and winter and spring averages in blue.

In Figure 11, we compare the net carbon flux poleward of a given latitude with the inferences of *Takahashi et al.* [2009] and *Landschützer et al.* [2015]. A major caveat is that the Takahashi product is an estimate calibrated to year 2000, whereas the B-SOSE and Landschutzer CO_2 fluxes represent years 2008 to 2011. Black curves show the annual mean fluxes, blue curves show the winter and spring averages, and orange curves show the summer and fall averages. The agreement between B-SOSE and *Landschützer et al.* [2015] is very good up to ∼55°S, at which point the summer-time B-SOSE outgassing causes the estimates to diverge. Compared to *Takahashi et al.* [2009], our estimate has less outgassing at high latitudes. Although the total integrated flux at 30°S is close to the *Takahashi et al.* [2009] value, this is partly due to the summer outgassing at midlatitudes in B-SOSE, which is possibly an overestimate.

5.2. Nitrate Transport

Another example of the use of the time-evolving biogeochemical state estimate is in investigating interior transports. Advection of nutrient-rich Intermediate Waters (IW) from the Southern Ocean is hypothesized to fertilize the low-latitude oceans [*Sarmiento et al.*, 2004; *Marinov et al.*, 2006]. Lateral transport of nitrate supplies between 17% and 24% of the upper-ocean nitrogen in the subtropical gyres of the South Atlantic, South Pacific, and Indian Oceans [*Letscher et al.*, 2016]; other sources are lateral transport of dissolved organic nitrogen, vertical transport, nitrogen fixation, and atmospheric deposition.

We quantify the export of nitrate out of the Southern Ocean in the IW layer (see definitions in Figure 12) across 32°S. The mean volume transport is 9.71 ± 5.07 Sv, 13.09 ± 6.77 Sv, and 7.51 ± 5.18 into the Atlantic, Indian, and Pacific Oceans (Figure 12). These Southern Ocean outflows carry different amounts of nitrate across 32°S, and while there is significant fertilization of the South Atlantic (5.57 ± 2.94 Tmol yr^{-1}) and Indian (5.09 ± 3.06 Tmol yr^{-1}) subtropical gyres, much less nitrate reaches the South Pacific (1.78 ± 1.91 Tmol yr^{-1}). The South Pacific does have the smallest IW inflow, and thus this low fertilization rate may be related to the physical circulation. However, the nutrient-rich ACC is farthest poleward in this sector, and there may be more nitrate utilization as these waters travel further to reach 32°S. Both volume and nitrate transport show significant variability at all resolved timescales. The sources of this variability and implications for observing strategy, warrant further study.

The magnitude of the nitrogen sinks in the upper ocean of the Southern Hemisphere subtropical gyres is estimated from the numbers given in *Letscher et al.* [2016] and our assumption that the gyres extend from 32°S to 10°S and from coast to coast: 2.1 Tmol yr^{-1} in the South Atlantic, 4.1 Tmol yr^{-1} in the Indian, and

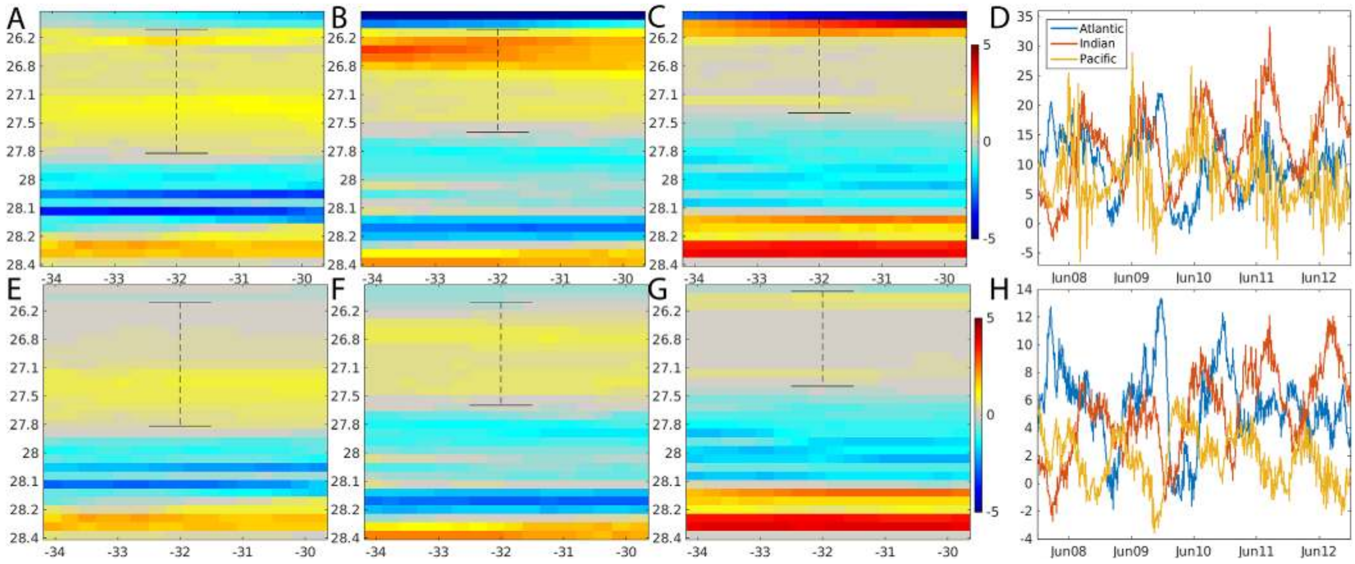

Figure 12. Volume transport in neutral density, γ, layers for the (a) Atlantic, (b) Indian, and (c) Pacific sectors of the Southern Ocean in Sv. Nitrate transport in γ-layers is shown below (e, f, g) in Tmol yr^{-1}. The transport is quantified across 32°S into the Atlantic Ocean for the IW layer $25.99 < \gamma < 27.76$, into the Indian Ocean for the IW layer $25.99 < \gamma < 27.55$, and into the Pacific for the IW layer $25.18 < \gamma < 27.34$ for (d) volume and (h) nitrate (layers denoted by a dashed black line). The mean volume transport is 9.71 ± 5.07, 13.08 ± 6.77, and 7.49 ± 5.17 Sv for the Atlantic, Indian, and Pacific Oceans, where the ± gives the standard deviation from the 3 day average time series. The nitrate volume transport for these three basins is 5.57 ± 2.94, 5.09 ± 3.06, and 1.78 ± 1.91 Tmol yr^{-1}, respectively.

4.7 Tmol yr^{-1} in the South Pacific. The B-SOSE transport estimates suggest that IW from the Southern Ocean could supply more than enough nutrients to fertilize the Atlantic and Indian subtropical gyres. Of course, some of the nutrients may not mix above the pycnocline to contribute to upper ocean budgets. For the South Pacific gyre, the B-SOSE estimate is smaller compared to the basin budget, though uncertainties on both numbers are large. It is possible that a high fraction of nutrients in IW reach the surface, or that upper-ocean nitrogen is coming from other sources. The mechanisms behind the transport of nitrate from the Southern Ocean to the subtropics should be explored through a thorough analysis of the nitrogen budget in B-SOSE.

6. Concluding Remarks

We demonstrate that adjoint method state estimation works in a coupled physical-biogeochemical framework. A 5 year estimate of the ocean state is produced, and validation shows it has good skill at fitting in situ observations of oxygen and of surface pCO$_2$ in Drake Passage. For those biogeochemical fields, which are constrained with the most year-round observations, the state estimate is as consistent with the data as currently published climatologies derived by objective mapping. An advantage of the state estimate over these products, however, is that the temporally evolving fields are dynamically consistent and have closed budgets for biogeochemical tracers. The B-SOSE product is available online with 3 day and monthly averaging periods. An extended assessment of its consistency with observations is also available. Lastly, the model setup and input files are also available.

Of course, the solution has limitations. Because observations of DIC, alkalinity, and pH are sparse and taken almost only during summer, the carbon system is under-constrained. Similarly, the biological pump is poorly constrained due to the paucity of nitrate, phosphate, and iron observations. The SOCATv4 data set is our best constraint of surface pCO$_2$ and air-sea CO$_2$ fluxes and has allowed us to derive an uncertainty estimate for our flux inference. These SOCATv4 observations suggest that the B-SOSE estimated pCO$_2$ may be too high in the subtropics and at midlatitudes. Nevertheless, other SOCATv4 observations, and the Drake Passage time series in particular, reveal that much of the variability is captured. As we move forward extending B-SOSE to near present, the Drake Passage pCO2 time series will continue to be a validation focal point. Being the best constrained region with an extended time series of observations makes this repeat line valuable for assessing model error.

A primary source of model error arises from the relatively simple representation of biological processes in BLING. For example, advection and diffusion of phytoplankton biomass is neglected. Since the adjoint method requires a high amount of computational resources, adding three additional prognostic fields (for the biomass of each phytoplankton type) would carry a significant cost. Instead, we are implementing a single variable representing the total biomass that is partitioned into different types based on local conditions; this will be tested for potential use in a future version of B-SOSE. We plan to take advantage of the adjoint machinery and extensive validation methodology to quantify the benefit of enhancing the realism of the biological model. Assessing the influence of model error (as opposed to model input error) may inform improvement of biogeochemical models of intermediate complexity, which are commonly used for studies of the climate system.

The adjoint model can also be used to investigate the processes governing Southern Ocean biogeochemistry through adjoint sensitivity experiments. Adjoint sensitivities are response functions revealing how the biogeochemistry at a given location is connected to various forcing mechanisms at all earlier times. Detailed analysis of the sensitivity patterns can be used to quantify the drivers of ocean carbon variability. For example, *Dutkiewicz et al*. [2006] used adjoint sensitivity experiments to map the influence of atmospheric iron input on biological production and air-sea fluxes of CO$_2$ in a coarse resolution global model. One also envisions using the adjoint-derived sensitivities plotted in Figure 3 to help understand observations taken in Drake Passage. Quantifying the sensitivity of the carbon system to momentum forcing, buoyancy forcing, and biological activity allows one to explore the links between ocean response and climate forcing.

Our next step will be working toward a 2013–2020 B-SOSE that will assimilate data from SOCCOM floats. We plan to add controls on parameters that regulate biological production: maximum photosynthesis rate, iron sensitivity, light sensitivity, and organic matter remineralization rates, for example. A central effort will be to analyze the state estimate to assess the variability and understand the sensitivity of the system. The

Argo array provided a drastic increase in temperature and salinity observations when it was first deployed in the Southern Ocean in 2004, transforming our knowledge of the physical state. The hope is that bgc-Argo will do the same for the Southern Ocean carbon cycle, and we have produced a methodology to synthesize these coming observations.

Acknowledgments
This work was sponsored by NSF's Southern Ocean Carbon and Climate Observations and Modeling (SOCCOM) Project under the NSF award PLR-1425989. Logistical support for this project in Antarctica was provided by the U.S. National Science Foundation through the U.S. Antarctic Program. We thank Joellen Russell and the University of Arizona for providing the computing resources to produce B-SOSE. We acknowledge use of multiple data products, referenced in the text. The MDT_CNES-CLS13 product used was produced by CLS Space Oceanography Division and distributed by Aviso, with support from Cnes (http://www.aviso.altimetry.fr). HYCOM output used was produced with funding provided by the National Ocean Partnership Program and the Office of Naval Research. Data assimilative products using HYCOM are funded by the U.S. Navy. Computer time was made available by the DoD High Performance Computing Modernization Program; the output is publicly available at http://hycom.org. The Surface Ocean CO_2 Atlas (SOCAT) is an international effort, endorsed by the International Ocean Carbon Coordination Project (IOCCP), the Surface Ocean Lower Atmosphere Study (SOLAS), and the Integrated Marine Biogeochemistry and Ecosystem Research program (IMBER), to deliver a uniformly quality-controlled surface ocean CO_2 database. The many researchers and funding agencies responsible for the collection of data and quality control are thanked for their contributions to SOCAT. Argo data were collected and made freely available by the International Argo Program and the national programs that contribute to it (http://www.argo.ucsd.edu, http://argo.jcommops.org). The Argo Program is part of the Global Ocean Observing System (http://doi.org/10.17882/42182). We thank Matthew Long, John Dunne, and Eric Galbraith for helpful discussions and advice on biogeochemical modeling, and Roberta Hotinski for logistical support. The input of two anonymous reviewers greatly improved this manuscript.

References

Amante, C., and B. W. Eakins (2009), ETOPO1 Global Relief Model converted to PanMap layer format, NOAA-National Geophysical Data Center, PANGAEA, doi:10.1594/PANGAEA.769615.

Bakker, D., E. McDonagh, M. Stinchcombe, and M. Messias (2013), Carbon dioxide, hydrographic, and chemical data obtained during the R/V James Cook JC031 Cruise in the South Atlantic Ocean on CLIVAR repeat hydrography Section A21 (SR1, SR1b) (3 February–3 March, 2009), Carbon Dioxide Inf. Anal. Cent., Oak Ridge Natl. Lab., U.S. Dep. of Energy, Oak Ridge, Tenn., doi:10.3334/CDIAC/OTG.CLIVAR_A21_JC031_2009. [Available at http://cdiac.ornl.gov/ftp/oceans/CLIVAR/A21_JC031/.]

Bakker, D. C. E., et al. (2016), A multi-decade record of high quality fCO_2 data in version 3 of the Surface Ocean CO_2 Atlas (SOCAT), *Earth Syst. Sci. Data*, *8*, 383–413, doi:10.5194/essd-8-383-2016.

Bianchi, D., E. D. Galbraith, D. A. Carozza, K. A. S. Mislan, and C. A. Stock (2013), Intensification of open-ocean oxygen depletion by vertically migrating animals, *J. Adv. Model. Earth Syst.*, *6*, 545–548, doi:10.1038/ngeo1837.

Bopp, L., et al. (2013), Multiple stressors of ocean ecosystems in the 21st century: Projections with CMIP5 models, *Biogeosciences*, *10*, 6225–6245, doi:10.5194/bg-10-6225-2013.

Bullister, J., R. Feely, R. Wanninkhof, A. Dickson, D. Hansell, and R. Key (2010), Carbon dioxide, hydrographic, and chemical data obtained during the R/V Ronald H. Brown Cruise in the Atlantic Ocean on CLIVAR Repeat Hydrography Section A13.5 (March 08–April 17, 2010), Carbon Dioxide Inf. Anal. Cent., Oak Ridge Natl. Lab., U.S. Dep. of Energy, Oak Ridge, Tenn., doi:10.3334/CDIAC/otg.CLIVAR_A13.5_2010. [Available at http://cdiac.ornl.gov/ftp/oceans/CLIVAR/A13.5_2010.data/.]

Dai, A., and K. E. Trenberth (2002), Estimates of freshwater discharge from continents: Latitudinal and seasonal variations, *J. Hydrometeorol.*, *3*(6), 660–687, doi:10.1175/1525-7541(2002)003<0660:EOFDFC>2.0.CO;2.

Dee, D. P., et al. (2011), The ERA-Interim reanalysis: Configuration and performance of the data assimilation system, *Q. J. R. Meteorol. Soc.*, *137*(656), 553–597.

Doi, T., S. Osafune, N. Sugiura, S. Kouketsu, A. Murata, S. Masuda, and T. Toyoda (2015), Multidecadal change in the dissolved inorganic carbon in a long-term ocean state estimation, *J. Adv. Model. Earth Syst.*, *7*, 1885–1900, doi:10.1002/2015MS000462.

Dunne, J., et al. (2013), GFDL's ESM2 global coupled climate-carbon Earth System Models Part II: Carbon system formulation and baseline simulation characteristics, *J. Clim.*, *26*, 2247–2267, doi:10.1175/JCLI-D-12-00150.1.

Dunne, J. P., R. A. Armstrong, A. Gnanadesikan, and J. L. Sarmiento (2005), Empirical and mechanistic models for the particle export ratio, *Global Biogeochem. Cycles*, *19*, GB4026, doi:10.1029/2004GB002390.

Dutkiewicz, S., M. J. Follows, P. Heimbach, and J. C. Marshall (2006), Controls on ocean productivity and air-sea carbon flux: An adjoint model sensitivity study, *Geophys. Res. Lett.*, *33*, L02603, doi:10.1029/2005GL024987.

Eppley, R. W. (1972), Temperature and phytoplankton growth in the sea, *Fish. Bull.*, *70*, 1063–1085.

Faugeras, B., M. Lévy, L. Mémery, J. Verronc, J. Blumd, and I. Charpentier (2003), Can biogeochemical fluxes be recovered from nitrate and chlorophyll data? A case study assimilating data in the Northwestern Mediterranean Sea at the JGOFS-DYFAMED station, *J. Mar. Syst.*, *40–41*, 99–125, doi:10.1016/S0924-7963(03)00015-0.

Fay, A. R., and G. A. McKinley (2014), Southern Ocean carbon trends: Sensitivity to methods, *Geophys. Res. Lett.*, *41*, 6833–6840, doi:10.1002/2014GL061324.

Fay, A. R., G. A. McKinley, and N. S. Lovenduski (2013), Global trends in surface ocean pCO_2 from in situ data, *Global Biogeochem. Cycles*, *27*, 541–557, doi:10.1002/gbc.20051.

Fennel, K., M. Losch, J. Schröter, and M. Wenzel (2001), Testing a marine ecosystem model: Sensitivity analysis and parameter optimization, *J. Mar. Syst.*, *28*, 45–63.

Fenty, I., and P. Heimbach (2012), Coupled sea ice-ocean-state estimation in the Labrador Sea and Baffin Bay, *J. Phys. Oceanogr.*, *43*(5), 884–904, doi:10.1175/JPO-D-12-065.1.

Follows, M. J., T. Ito, and S. Dutkiewicz (2006), On the solution of the carbonate chemistry system in ocean biogeochemistry models, *Ocean Modell.*, *12*(3–4), 290–301, doi:10.1016/j.ocemod.2005.05.004.

Forget, G., J.-M. Campin, P. Heimbach, C. N. Hill, R. M. Ponte, and C. Wunsch (2015), ECCO version 4: An integrated framework for non-linear inverse modeling and global ocean state estimation, *Geosci. Model Dev.*, *8*(10), 3071–3104, doi:10.5194/gmd-8-3071-2015.

Friedrichs, M. A. M., R. R. Hood, and J. D. Wiggert (2006), Ecosystem model complexity versus physical forcing: Quantification of their relative impact with assimilated Arabian Sea data, *Deep Sea Res., Part II*, *53*(5–7), 576–600, doi:10.1016/j.dsr2.2006.01.026.

Galbraith, E. D., A. Gnanadesikan, J. P. Dunne, and M. R. Hiscock (2010), Regional impacts of iron-light colimitation in a global biogeochemical model, *Biogeosciences*, *7*, 1043–1064.

Galbraith, E. D., et al. (2015), Complex functionality with minimal computation: Promise and pitfalls of reduced-tracer ocean biogeochemistry models, *J. Adv. Model. Earth Syst.*, *7*, 2012–2028, doi:10.1002/2015MS000463.

Garcia, H. E., R. A. Locarnini, T. P. Boyer, J. I. Antonov, O. Baranova, M. M. Zweng, J. R. Reagan, and D. R. Johnson (2014a), World Ocean Atlas 2013, volume 3: Dissolved oxygen, Apparent Oxygen Utilization, and Oxygen Saturation, NOAA Atlas NESDIS, 75, 27.

Garcia, H. E., R. A. Locarnini, T. P. Boyer, J. I. Antonov, O. Baranova, M. M. Zweng, J. R. Reagan, and D. R. Johnson (2014b), World Ocean Atlas 2013, volume 4: Dissolved Inorganic Nutrients (Phosphate, Nitrate, Silicate), NOAA Atlas NESDIS, 76, 25.

Gaspar, P., Y. Grégoris, and J.-M. Lefevre (1990), A simple eddy kinetic energy model for simulations of the oceanic vertical mixing: Tests at station papa and long-term upper ocean study site, *J. Geophys. Res.*, *95*(C9), 16,179–16,193, doi:10.1029/JC095iC09p16179.

Gilbert, J. C., and C. Lemaréchal (1989), Some numerical experiments with variable-storage quasi-Newton algorithms, *Math. Program.*, *45*, 407–435.

Gruber, E. A. N. (2009), Oceanic sources, sinks, and transport of atmospheric CO_2, *Global Biogeochem. Cycles*, *23*, GB1005, doi:10.1029/2008GB003349.

Hammond, M. D., and D. Jones (2016), Freshwater flux from ice sheet melting and iceberg calving in the Southern Ocean, *Geosci. Data J.*, *3*, 60–62, doi:10.1002/gdj3.43.

Jiang, C. L., S. T. Gille, J. Sprintall, and C. Sweeney (2014), Drake Passage oceanic pCO_2: Evaluating CMIP5 coupled carbon-climate models using in situ observations, *J. Clim.*, *27*, 76–100, doi:10.1175/JCLI-D-12-00571.1.

Johnson, K., J. Plant, L. Talley, and J. Sarmiento (2017), Annual nitrate drawdown observed by SOCCOM profiling floats and the relationship to annual net community production, *J. Geophys. Res. Oceans*, doi:10.1002/2017JC012839.

Key, R., et al. (2015), Global Ocean Data Analysis Project, Version 2 (GLODAPv2), *ORNL/CDIAC-162, ND-P093*, Carbon Dioxide Inf. Anal. Cent., Oak Ridge Natl. Lab., U.S. Dep. of Energy, Oak Ridge, Tenn., doi:10.3334/CDIAC/OTG.NDP093_GLODAPv2.

Khatiwala, S., F. Primeau, and T. Hall (2009), Reconstruction of the history of anthropogenic CO_2 concentrations in the ocean, *Nature*, *462*, 346–349, doi:10.1038/nature08526.

Khatiwala, S., T. Tanhua, S. M. Fletcher, M. Gerber, S. C. Doney, H. D. Graven, and N. Gruber (2013), Global ocean storage of anthropogenic carbon, *Biogeosciences*, *10*, 2169–2191, doi:10.5194/bg-10-2169-2013.

Landschützer, P., et al. (2015), The reinvigoration of the Southern Ocean carbon sink, *Science*, *349*, 1221–1224, doi:10.1126/science.aab2620.

Large, W. G., and S. G. Yeager (2009), The global climatology of an interannually varying air-sea flux data set, *Clim. Dyn.*, *33*, 341–364.

Lauvset, S. K., et al. (2016), A new global interior ocean mapped climatology: The 1° × 1° GLODAP version 2, *Earth Syst. Sci. Data*, *8*, 325–340, doi:10.5194/essd-8-325-2016.

Le Quéré, C. (2010), Trends in the land and ocean carbon uptake, *Curr. Opin. Environ. Sustainability*, *2*, 219–224.

Le Quéré, C., et al. (2007), Saturation of the Southern Ocean CO_2 sink due to recent climate change, *Science*, *316*, 1735–1738.

Le Quéré, C., T. Takahashi, E. T. Buitenhuis, C. Rödenbeck, and S. C. Sutherland (2010), Impact of climate change and variability on the global oceanic sink of CO_2, *Global Biogeochem. Cycles*, *24*, GB4007, doi:10.1029/2009GB003599.

Letscher, R. T., F. Primeau, and J. K. Moore (2016), Nutrient budgets in the subtropical ocean gyres dominated by lateral transport, *Nature*, *9*, 815–819, doi:10.1038/NGEO2812.

Losch, M., D. Menemenlis, J.-M. Campin, P. Heimbach, and C. Hill (2010), On the formulation of sea-ice models. Part 1: Effects of different solver implementations and parameterizations, *Ocean Modell.*, *33*(1–2), 129–144.

Lovenduski, N. S., M. C. Long, P. R. Gent, and K. Lindsay (2013), Multi-decadal trends in the advection and mixing of natural carbon in the southern ocean, *Geophys. Res. Lett.*, *40*, 139–142, doi:10.1029/2012GL054483.

Lovenduski, N. S., A. R. Fay, and G. A. McKinley (2015), Observing multidecadal trends in Southern Ocean CO_2 uptake: What can we learn from an ocean model?, *Global Biogeochem. Cycles*, *29*, 416–426, doi:10.1002/2014GB004933.

Mahowald, N. M., A. R. Baker, G. Bergametti, N. Brooks, R. A. Duce, T. D. Jickells, N. Kubilay, J. M. Prospero, and I. Tegen (2005), Atmospheric global dust cycle and iron inputs to the ocean, *Global Biogeochem. Cycles*, *19*, GB4025, doi:10.1029/2004GB002402.

Majkut, J. D., J. L. Sarmiento, and K. B. Rodgers (2014), A growing oceanic carbon uptake: Results from an inversion study of surface pCO_2 data, *Global Biogeochem. Cycles*, *28*, 335–351, doi:10.1002/2013GB004585.

Marinov, I., A. Gnanadesikan, R. Toggweiler, and J. Sarmiento (2006), The Southern Ocean biogeochemical divide, *Nature*, *441*, 964–967, doi:10.1038/nature04883.

Marshall, J., A. Adcroft, C. Hill, L. Perelman, and C. Heisey (1997), A finite-volume, incompressible Navier Stokes model for studies of the ocean on parallel computers, *J. Geophys. Res.*, *102*(C3), 5753–5766.

Mattern, J., H. Song, C. Edwards, A. Moore, and J. Fiechter (2017), Data assimilation of physical and chlorophyll a observations in the California Current System using two biogeochemical models, *Ocean Modell.*, *109*, 55–71, doi:10.1016/j.ocemod.2016.12.002.

Matear, R. J. (1995), Parameter optimization and analysis of ecosystem models using simulated annealing: A case study at Station P, *J. Mar. Res.*, *53*(4), 571–607, doi:10.1357/0022240953213098.

Mawji, E., et al. (2015), The GEOTRACES Intermediate Data Product 2014, *Mar. Chem.*, *177*, 1–8, doi:10.1016/j.marchem.2015.04.005.

Mazloff, M. R., P. Heimbach, and C. Wunsch (2010), An eddy-permitting southern ocean state estimate, *J. Phys. Oceanogr.*, *40*(5), 880–899, doi:10.1175/2009JPO4236.1.

McKinley, G. A., A. R. Fay, N. S. Lovenduski, and D. J. Pilcher (2017), Timescales for detection of trends in the ocean carbon sink, *Annu. Rev. Mar. Sci.*, *9*, 125–150, doi:10.1146/annurev-marine-010816-060529.

Meier, W., F. Fetterer, M. Savoie, S. Mallory, R. Duerr, and J. Stroeve (2013, updated 2016), NOAA/NSIDC Climate Data Record of Passive Microwave Sea Ice Concentration, Version 2, doi:10.7265/N55M63M1.

Metzl, N. (2009), Decadal increase of oceanic carbon dioxide in Southern Indian Ocean surface waters (1991–2007), *Deep Sea Res., Part II*, *56*, 607–619, doi:10.1016/j.dsr2.2008.12.007.

Munro, D. R., N. S. Lovenduski, T. Takahashi, B. B. Stephens, T. Newberger, and C. Sweeney (2015a), Recent evidence for a strengthening CO_2 sink in the Southern Ocean from carbonate system measurements in the Drake Passage (2002–2015), *Geophys. Res. Lett.*, *42*, 7623–7630, doi:10.1002/2015GL065194.

Munro, D. R., N. Lovenduski, B. Stephens, T. Newberger, K. Arrigo, T. Takahashi, P. Quay, J. Printall, N. Freeman, and C. Sweeney (2015b), Estimates of net community production in the Southern Ocean determined from time series observations (2002–2011) of nutrients, dissolved inorganic carbon, and surface ocean pCO_2 in Drake Passage, *Deep Sea Res., Part II*, *114*, 49–63, doi:10.1016/j.dsr2.2014.12.014.

Nocedal, J. (1980), Updating quasi-Newton matrices with limited storage, *Math. Comput.*, *35*, 773–782.

Olsen, A., et al. (2016), The Global Ocean Data Analysis Project version 2 (GLODAPv2)—An internally consistent data product for the world ocean, *Earth Syst. Sci. Data*, *8*, 297–323, doi:10.5194/essd-8-297-2016.

Orsi, A. H., T. Whitworth III, and W. D. Nowlin Jr. (1995), On the meridional extent and fronts of the Antarctic circumpolar current, *Deep Sea Res., Part I*, *42*, 641–673.

Peters, W., et al. (2007), An atmospheric perspective on North American carbon dioxide exchange: CarbonTracker, *Proc. Natl. Acad. Sci. U. S. A.*, *104*(48), 18,925–18,930.

Plant, J. N., K. S. Johnson, C. M. Sakamoto, H. W. Jannasch, L. J. Coletti, S. C. Riser, and D. D. Swift (2016), Net community production at ocean station papa observed with nitrate and oxygen sensors on profiling floats, *Global Biogeochem. Cycles*, *30*(6), 859–879, doi:10.1002/2015GB005349.

Roemmich, D., and J. Gilson (2009), The 2004–2008 mean and annual cycle of temperature, salinity, and steric height in the global ocean from the Argo Program, *Prog. Oceanogr.*, *82*, 81–100.

Sallée, J. B., E. Shuckburgh, N. Bruneau, A. J. S. Meijers, T. J. Bracegirdle, Z. Wang, and T. Roy (2013), Assessment of Southern Ocean water mass circulation and characteristics in CMIP5 models: Historical bias and forcing response, *J. Geophys. Res. Oceans*, *118*, 1830–1844, doi:10.1002/jgrc.20135.

Sarmiento, J. L., N. Gruber, M. A. Brzezinski, and J. P. Dunne (2004), High-latitude controls of thermocline nutrients and low latitude biological productivity, *Nature*, *427*, 56–60, doi:10.1038/nature02127.

Schlitzer, R. (2002), Carbon export fluxes in the Southern Ocean: Results from inverse modeling and comparison with satellite-based estimates, *Deep Sea Res., Part II*, *49*(9–10), 1623–1644, doi:10.1016/S0967-0645(02)00004-8.

Song, H., C. A. Edwards, A. M. Moore, and J. Fiechter (2012), Incremental four-dimensional variational data assimilation of positive-definite oceanic variables using a logarithm transformation, *Ocean Modell.*, *54–55*, 1–17, doi:10.1016/j.ocemod.2012.06.001.

Song, H., C. A. Edwards, A. M. Moore, and J. Fiechter (2016a), Data assimilation in a coupled physical-biogeochemical model of the California Current System using an incremental lognormal 4-dimensional variational approach: Part 1-Model formulation and biological data assimilation twin experiments, *Ocean Modell.*, *106*, 131–145, doi:10.1016/j.ocemod.2016.04.001.

Song, H., C. A. Edwards, A. M. Moore, and J. Fiechter (2016b), Data assimilation in a coupled physical-biogeochemical model of the California Current System using an incremental lognormal 4-dimensional variational approach: Part 3—Assimilation in a realistic context using satellite and in situ observations, *Ocean Modell.*, *106*, 131–145, doi:10.1016/j.ocemod.2016.06.005.

Stammer, D., C. Wunsch, R. Giering, C. Eckert, P. Heimbach, J. Marotzke, A. Adcroft, C. N. Hill, and J. Marshall (2002), Global ocean circulation during 1992–1997, estimated from ocean observations and a general circulation model, *J. Geophys. Res.*, *107*(C9), 3118, doi:10.1029/2001JC000888.

Takahashi, T., et al. (2009), Climatological mean and decadal change in surface ocean pCO_2, and net sea-air CO_2 flux over the global oceans, *Deep Sea Res., Part II*, *56*, 554–577, doi:10.1016/j.dsr2.2008.12.009.

Takahashi, T., C. Sweeney, B. Hales, D. W. Chipman, T. Newberger, J. G. Goddard, R. A. Iannuzzi, and S. C. Sutherland (2012), The changing carbon cycle in the Southern Ocean, *Oceanography*, *3*, 26–37, doi:10.1016/j.dsr2.2008.12.009.

Wanninkhof, R. (1992), Relationship between wind speed and gas exchange, *J. Geophys. Res.*, *97*(C5), 7373–7382.

Williams, N. L., et al. (2017), Calculating surface ocean pCO_2 from biogeochemical Argo floats equipped with pH: An uncertainty analysis, *Global Biogeochem. Cycles*, *31*, 591–604, doi:10.1002/2016GB005541.

Wunsch, C., and P. Heimbach (2007), Practical global oceanic state estimation, *Physica D*, *230*(1–2), 197–208, doi:10.1016/j.physd.2006.09.040.

Wunsch, C., and P. Heimbach (2013), Dynamically and kinematically consistent global ocean circulation and ice state estimates, in *Ocean Circulation and Climate*, edited by J. Siedler et al., 2 ed., vol. 103 of International Geophysics, pp. 553–580, Academic Press, Oxford, U. K.